Engineered Noble-metal Nanostructures for In Vitro Diagnostics

Zheng Xi,† Haihang Ye† and Xiaohu Xia†,*

Abstract

The unique properties of engineered noble-metal nanostructures make them versatile and robust signal transducers for *in vitro* diagnostics (IVDs). Particularly, thanks to the increased mechanistic understanding on fundamental nano-research and the rapid advancement of high-performance analytical tools, it is now feasible to tightly tune the physical and chemical parameters (including size, shape, elemental composition, and internal structure) of a noble-metal nanostructure at the atomic precision. Through careful control over these parameters, one can optimize the physicochemical properties of a metal nanostructure and thereby enhance its performance in IVDs. In this article, we introduce recently developed methodologies for effectively engineering noble-metal nanostructures with desired properties, discuss the superior performance of the engineered nanostructures in various IVD platforms, and provide insights into materials design, synthesis, and application in IVDs. We hope this article will serve as a useful foundation to inspire future research in this emerging niche field.

Detection Signal Metal Nanostructure

Biomarker

Table of Contents

Keywords: Noble metal · nanostructure · controlled synthesis · *in vitro* diagnostics · biomarkers

[†]Department of Chemistry, University of Central Florida, Orlando, Florida 32816, United States

^{*}Corresponding author. E-mail: Xiaohu.Xia@ucf.edu

1. Introduction

1.1. In Vitro Diagnostics (IVDs) and Their Significance

In vitro diagnostics (IVDs) refer to tests on biological samples that are taken from the human body, including, but not limited to, blood, urine, saliva, and tissues. ¹⁻⁴ IVD tests are usually performed to detect and monitor disease in an individual (in most cases, through the determination of molecular biomarkers), intending to provide valuable medical information for disease treatment, management, and prevention. IVDs represent a crucial component in modern healthcare. They influence more than 60% of clinical decision making, while accounting for only ~2% of total healthcare spending. ⁵ IVDs reduce cost by diminishing subsequent health issues, avoiding unnecessary treatment, and reducing hospitalization. In addition to cost-effectiveness, IVDs are featured by low patient risk. Most IVDs do not come into direct contact with human body, involving no more than minimal risk for a patient. ⁶⁻⁸

Today, IVDs go far beyond simply telling a doctor whether a patient has certain diseases or not. They are able to spot early warning signs, provide quantitative data on relevant biomarkers, and evaluate individual risk factors. ^{9, 10} This information greatly enhances doctors' ability to make an optimized decision at the right time. The versatile capabilities of IVDs make them an integral part of decision making during the entire continuum of patient care. For instance, in dealing with cancers, IVDs can guide physicians to make clinical decisions on both treatment and recovery. Prior to any invasive treatments, IVD tests (*e.g.*, blood tests for prostate cancer and core-needle biopsy for breast cancer) need to be performed to obtain detailed information about cancer, such as the exact kind of cancer, the stage of cancer, and how fast it is expanding. After treatment, IVDs help physicians monitor possible cancer recurrence by measuring the level of specific biomarkers in a patient's blood or tissue. ¹¹⁻¹⁵

The increasing demand of IVDs and their significance in biomedicine drive the development of new IVD technologies towards higher sensitivity, greater simplicity, and lower cost. In particular, high sensitivity is critical in early detection of life-threatening diseases such as cancers, infectious diseases, and cardiovascular disease, creating opportunities for early intervention and prevention. Great simplicity and low cost allow IVDs to extend beyond clinical laboratory and doctor's office, empowering patients to self-monitor and manage their own health conditions and ultimately achieving sustainable healthcare. ^{20, 21}

1.2. Noble-metal Nanostructures in IVDs

Nanostructures of noble metals (including Au, Ag, Pt, Pd, Rh, Ir, and Ru) as a group of emerging functional materials have received increasing interest in various fields over the past several decades.²²⁻³⁰ The unique and intriguing physicochemical properties of noble-metal nanostructures make them attractive for IVDs.^{6, 31-34} For example, i) They offer multiple signal transduction principles suited for efficient IVD tests. They can generate various types of signal such as optical, 35 plasmonic, 36 electrochemical, 37, 38 surface-enhanced Raman scattering (SERS), 39, ⁴⁰ fluorescent, ^{41, 42} and colorimetric signal. ^{43, 44} Notably, a very small amount of noble-metal nanostructures are required to yield a strong signal, allowing for sensitive detection; ii) Owing to the great efforts by many research groups in the past, 45-49 they can now be produced in high quality and large quantities, ensuring good reproducibility for associated IVDs; iii) Their surface can be conveniently modified with functional groups such as amino and carboxyl groups by means of metal-thiolate bonding, allowing for facile label of biomolecules (e.g., antibodies and nucleic acids); 50-53 iv) They are made of noble metals with excellent stability and mechanical flexibility, enabling them to easily survive complex and harsh environments. 54-56 This feature is particularly desired for point-of-care IVDs, where environmental conditions such as temperature, humidity, and air quality are less predictable and controllable than those in a clinical laboratory. 57-59 Finally, it should be noted that the cost of noble metals should not be an issue in this particular application because of the tiny amount of materials usage in IVDs.

Technological advancement is oftentimes driven by scientific discoveries. Putting these functional noble-metal nanostructures to work for revolution of IVD technologies is an exciting task for scientists worldwide. However, the path from lab experiments to clinical use is long and fraught with pitfalls. The lack of in-depth fundamental understanding and difficulties in dealing with complicated clinical samples make the translational period of these nanostructures in IVDs rather arduous. Nevertheless, a few of them have already made it through. For example, Au nanoparticles-based test strip technology has successfully been brought to the market since the 1980s and become a powerful tool to solve real-world problems (*e.g.*, tests for pregnancy and malaria). 60-62 It is worth mentioning that facile and scalable synthesis of quality colloidal Au nanoparticles can be traced back to the work by Turkevich *et al.* in the early 1950s 63-65 – only ~30 years behind the practical use. Over the past two decades, great progress has been made on both fundamental and practical sides of noble-metal nanostructures. It is now feasible to manufacture noble-metal nanostructures with good uniformities and commercial scales. 66-71 Taken together, this

niche field is primed to make the transition from scientific findings to clinical realities.

1.3. What is Unique about "Engineered"?

In this article, the term "engineered" refers to noble-metal nanomaterials "with controlled physical parameters, including size, shape, elemental composition, and internal structure (*i.e.*, type of crystallinity and degree of hollowness)". It is well documented that the physicochemical properties of a noble-metal nanostructure have strong dependence on these physical parameters.^{30,} For a specific application, one can tailor the properties and optimize the performance of metal nanostructure by carefully tuning one of these parameters, or a combination of them.

For example, the molar absorptivity of Au nanospheres is enlarged by 1,000 times when the diameter of sphere is increased from 5 to 50 nm. 80,81 In another example, for Ag nanospheres of 50 nm in diameter, the localized surface plasmon resonance (LSPR) is dominated by a strong peak at ~450 nm, giving their aqueous suspension a distinct yellow color since the purple/blue color of incident light is largely absorbed by the nanospheres. 82-84 Interestingly, when the spheres are reshaped to rods with dimensions of 20 × 50 nm² (width × length), their major LSPR peak is shifted to ~600 nm. 85 As a result, the aqueous suspension of these nanorods displays a striking blue color. In heterogeneous catalysis, the specific activity of Pt nanoparticles toward oxygen reduction reaction could be enhanced by approximately 10 times by incorporating Pt with another element – Ni to form an alloy of Pt₃Ni. 86, 87 Pd icosahedra with multiple twin defects showed a catalytic activity towards formic-acid oxidation that was several times higher than single-crystal Pd octahedrons with a similar size. 88, 89

These and many other examples clearly demonstrate the critical importance of "engineered" to the effective utilization of noble-metal nanostructures. Nevertheless, compared to other fields (*e.g.*, catalysis and *in vivo* biomedicine^{30, 90-93}), engineered noble-metal nanostructures have not been extensively studied in IVDs. Only within the last few decades have them been applied to IVD tests. On the other hand, with our increased mechanistic understanding and recent advancement in analytical tools, it is now practicable to precisely control the physical parameters of noble-metal nanostructures at the atomic level. 94-98 Collectively, it is particular excitement in regard to the application of engineered noble-metal nanostructures in IVDs.

1.4. Scope and Organization of the Article

This article aims to illustrate how engineering the physical parameters (size, shape, etc.) of a noble-metal nanostructure can enhance its performance in IVD tests. We discuss various

engineered noble-metal nanostructures used in IVDs, with a minimal discussion of conventional nanoparticles with an overall spherical shape. Since the topic of controlled synthesis of nanostructures is quite broad, we limit our discussion to solution-phase synthesis, ^{49, 99} where seeded growth (or seed-mediated growth, ¹⁰⁰⁻¹⁰⁴ see Section 2.1) as a highly effective approach is emphasized. Production of quality seeds from one-pot synthesis is not specified as it can be documented in literatures. ^{48, 49, 105} As limited by space, we only highlight the most effective strategy along with a few examples for each one of the controlled syntheses. Detailed synthetic approaches and mechanistic understandings can be found in our recently published review articles. ^{47, 106, 107} This article is organized by introducing the impacts of size, shape, elemental composition, and internal structure, one by one, on the performance of noble-metal nanostructures in IVDs. While we focus on engineered individual nanostructures, strategies based on nanoparticle aggregates, nanocrystal growth process, and chemical etching are also briefly accounted at the end of the article. In this article, we only discuss recent advancements of nanomaterials and IVD techniques made in the 2010s.

2. Impact of Size

2.1. Seeded Growth

Figure 1A illustrates a typical seeded growth of colloidal noble-metal nanostructures. Wherein, metal precursor solution is added to (in many cases, through a syringe pump) a vessel containing pre-formed seeds, reductant, capping agent and/or colloidal stabilizer that is placed in an oil or water bath equipped with a temperature controller. The precursor is reduced to metal atoms and then heterogeneously nucleate on the surface of seeds. Continued growth of seeds under a specific pathway results in the formation of desired nanostructures as the final products.

The growth pathway of a seed is controlled by a set of thermodynamic (*e.g.*, surface capping and reduction potential) and kinetic (*e.g.*, reagent concentration and temperature) parameters.⁴⁷ To understand the difference between thermodynamic and kinetic controls, consider two possible products (I and II) that may be obtained from the growth of a seed.¹⁰⁸⁻¹¹⁰ Product I is formed with a lower total free energy relative to product II. Therefore, product I is more thermodynamically stable. However, the activation energy barrier involved in the formation of product I is higher than that in the formation of product II. In this case, product I is expected when the synthesis is performed under thermodynamic control while product II will be favored if the synthesis is

switched to kinetic control. It should be pointed out that, despite thermodynamic and kinetic parameters are oftentimes intricately entangled to each other, one can determine which one takes the dominant role in a synthesis. More details about the fundamentals of seeded growth and thermodynamic/kinetic controls can be found in our recently published articles.^{47, 107} In following discussion, we will not elaborate on these concepts.

2.2. Control of Size

The size of nanostructures can be conveniently controlled in seeded growth by varying the ratio of metal precursor to seed. In principle, variation of precursor-to-seed ratio could be achieved by altering either the amount of precursor or the number of seeds (see Figure 1B). The key to a successful size-controlled synthesis is to carefully control the thermodynamic and kinetic parameters in a reaction to ensure that the original shape of seeds is maintained during the entire course of growth.

The capability of seeded growth in size control has been demonstrated in a number of noble metals. Taking Au nanospheres as a simple and important example, seeded growth allowed for a tight control of size in the range of 10-150 nm. In a set of synthesis, HAuCl4 solution (precursor to Au) was added to an aqueous solution containing a mixture of ascorbic acid (AA) as the reductant, 10 nm single-crystal Au spheres as the seeds, and cetyltrimethylammonium chloride (CTAC) as the stabilizer. As shown by Figure 1C, Au nanospheres with average diameters of 15, 46, and 80 nm could be obtained by reducing the number of seeds introduced to the synthesis while fixing the amount of precursor. By repeating the growth process and using the 46 nm Au nanospheres as the seeds, larger Au spheres with diameters of up to 150 nm could be obtained with high yields and narrow size distributions. The success of this synthesis relies on a slow reduction rate of Au³⁺ by AA, which allows for an adequately long period of time for the system to attain the global minimum in Gibbs free energy. As a result, sphere as a thermodynamically stable shape was maintained during the seeded growth.

In another example, Ag nanocubes with controlled edge lengths in the range of 30-200 nm could be synthesized in high yield through seeded growth. Different from the above Au nanosphere system, an alternative approach – adjusting the amount of precursor (AgNO₃ in this case) while fixing the number of seeds – was used to control the size. As shown in Figure 1D, Ag nanocubes with average edge lengths of 36, 99, and 172 nm, respectively, were obtained by increasing the amount of AgNO₃ solution in a standard synthesis from 10 to 75, and 200 μL. For

this synthesis, the key to the maintenance of cubic shape was to involve sufficient poly(vinylpyrrolidone) (PVP) molecules in the reaction solution. PVP as a Ag{100} facet-specific capping agent (see more details about capping agent in Section 3.1) can effectively and constantly passivate the newly formed Ag{100} facets during the growth, 113, 114 promoting the formation of six {100} facets-covered Ag nanocube as the final product.

2.3. Size-controlled Nanostructures in IVDs

Size plays a critical role in determining the performance of a noble-metal nanostructure in IVDs. It not only has a great impact on signal transduction but also affects the way a nanostructure interacts with biomolecules and/or other components of an IVD platform.

Surface plasmon resonance (SPR) biosensor as a widely used and commercially available IVD technology is a good example to illustrate the role and importance of particle size. SPR is a classic optical phenomenon that arises from the collective oscillation of surface conduction electrons of a metal (e.g., Au and Ag) in response to the oscillating electric field of incident light. 115-117 When the size of metal is shrunk to the nanoscale, the interaction between electron and light will be localized on the nanoparticle surface, which is termed the localized SPR (LSPR).⁷⁷ The principle of a conventional SPR biosensor relies on the fact that the binding of specific biomolecules onto the surface of a metal film can induce a variation in the dielectric constant, causing a change in the reflection of laser from a metal-liquid surface. 118 Since Au nanoparticles are highly sensitive to the dielectric constant of surrounding medium, they have been extensively used in SPR biosensors to amplify the SPR signal and enhance the detection sensitivity. 119, 120 In following discussion, Au nanoparticles with an overall spherical shape will be referred to as "AuNPs" for simplicity. It has been well recognized that the size of AuNP has a direct impact on their performance in SPR biosensors. For example, Liu et al. immobilized AuNPs of 500 and 60 nm in diameters on glass substrate for detecting cancer cells. 121 The results indicated that large-sized AuNPs have a longer electromagnetic field decay length, providing a broader linear range and higher sensitivity than those of small AuNPs ($\sim 10^3$ - 10^6 cells/mL for 500 nm AuNPs versus $\sim 10^4$ - 10^5 cells/mL for 60 nm AuNPs). He et al. observed that 45 nm AuNPs on a SiO₂-coated SPR chip gave a similar sensor response as 12 nm AuNPs, because the surface density of larger AuNPs was 20 times smaller than that of smaller ones. 122 Halpern et al. adsorbed AuNPs with diameters in the range of 20 to 100 nm onto a gold film and found that the sensor response increased with the size of AuNPs. 123

In a recent work, Springer et al. quantitatively investigated how the size of AuNPs influences

their capability in enhancing the response of SPR biosensors.¹²⁴ The study involved both experimental work and theoretical simulations. As a model system (Figure 2A), neutravidin-functionalized AuNPs (N-AuNPs) were used in the last step of a sandwich assay of carcinoembryonic antigen (CEA) to enhance the SPR sensor response to biotinylated secondary antibody against CEA. AuNPs with diameters of 10, 15, 21, 33, 52 nm were tested in this system to investigate the size effect. The sensor response (shift in the SPR wavelength, $\Delta \lambda_r$) is determined by two factors – the surface density of captured AuNPs ($\Delta \sigma$) and the sensor sensitivity to AuNP surface density (S_{σ}), which are related as $\Delta \lambda_r = \Delta \sigma \cdot S_{\sigma}$.

Herein, the first factor ($\Delta\sigma$) is defined as the ability of the N-AuNPs to bind to the SPR sensor surface through the interaction between biotinylated antibody and neutravidin on AuNP surface (Figure 2A). The second factor (S_{σ}) is defined only by the optical properties of both the N-AuNPs and the properties of the sensor. This factor measures the ratio between changes in the sensor response to changes in the N-AuNP surface density. Significantly, $\Delta\lambda_{\rm r}$ and $\Delta\sigma$ could be experimentally determined through SPR instrument readout and scanning electron microscopy (SEM) imaging, respectively. Therefore, the value of S_{σ} can be experimentally derived through following equation:

$$S_{\sigma} = \Delta \lambda_r / \Delta \sigma \tag{1}$$

The data of $\Delta\lambda_r$ and $\Delta\sigma$ for different sized AuNPs are summarized in Figure 2B and C, respectively. On the basis of these data and equation 1, the values of S_σ were derived (symbol \blacksquare in Figure 2D). This set of experimental data was well correlated to the results from a theoretical model (lines in Figure 2D) that relates the enhancement generated by various characteristics of the AuNPs (*e.g.*, size, composition, and concentration). It can be concluded that, while S_σ increases with the size of the N-AuNP, the ability of bioreceptors-functionalized surface of the sensor to bind the N-AuNPs is affected by steric effects and thus decreases with the size of N-AuNP. This study provides quantitative understanding on the impact of particle size, allowing for the design and development of SPR biosensors with optimized analytical performance.

Size also plays a decisive role in other signal transduction principles. Here we still use AuNPs as a type of representative nanostructure. AuNPs can effectively generate color signal (through absorption/scattering of incident light) and thermal contrast signal (through the photothermal effect^{125, 126}). Size of AuNPs has been recognized to have great impacts on both types of signal and associated IVD platforms. In a recent work by Zhan *et al.*, such impacts have been understood

from both theoretical and experimental aspects using lateral flow assay (LFA) as a model IVD platform. LFA is one of the most widely used and commercially available point-of-care IVD technologies. Nevertheless, its relatively low detection sensitivity (~1,000-times less sensitive than laboratory tests 129, 130) inhibits many critical applications such as early detection of significant cancers and acute infectious diseases.

In a typical sandwich LFA test (Figure 3A), analyte flows through a paper-based strip by capillary force and first captured by detection antibodies-labeled AuNPs to form a complex. The complex is then captured by antibodies pre-coated on the test zone of membrane. The accumulation of AuNPs at the test zone results in a visible red color, indicating a positive test. In conventional LFA, AuNPs of 30-40 nm in diameter are used as colorimetric labels. To improve the sensitivity of LFA, Zhan *et al.* carefully studied the impact of AuNP size (30, 60, and 100 nm in diameter). The nitrocellulose membrane is conceptually simplified as a bundle of cylindrical pores of radius R (Figure 3A). The Peclet number (Pe) and the Damkohler number (Da) were scaled to assess the importance of diffusion to convection and reaction in LFA (Figure 3B). Particularly, in the formula of Da, the effective forward reaction rate constant (k_{on}) for antibody-labeled AuNP is assumed to be:

$$k_{\rm on}' = nk_{\rm on}$$
 (2)

Wherein, k_{on} is the forward rate constant for a single antibody-antigen interaction in the LFA setting, and n is the effective number of antibodies per AuNP. A COMSOL model was developed to analyze the system and predict LFA performance prior to experiments. The model shows that reaction and convection have a higher impact on AuNP capture in test zone than diffusion, with reaction being the rate-limiting factor in AuNP capture. In this system, the reaction is largely determined by k_{on} . Therefore, on the basis of equation 2, larger sized AuNPs would have greater k_{on} due to the larger number of antibodies per AuNP (n) and thus could improve AuNP capture. Figure 3C shows the modeling results for a sandwich LFA of C-reactive protein (CRP, a biomarker of inflammation) achieved by the COMSOL model. Figure 3D shows the modeling results-guided experimental results where both thermal and color signals were measured for the CRP LFAs. It can be seen that the modeling results agreed well with experimental results, including the observation of the "hook effect" (reduction in signal at excessively high analyte concentrations ¹³¹. The two sets of data quantitatively demonstrate that larger sized AuNPs having a higher effective forward rate constant (k_{on}) could increase AuNP capture and therefore LFA sensitivity.

In particular, under thermal signal detection mode, 100 nm AuNPs yields a 256-fold sensitivity enhancement relative to conventional 30 nm AuNP-based colorimetric LFA. It should be mentioned that AuNP capture will be rate-limited by diffusion when the size is beyond 100 nm. Modeling results show that larger AuNPs (*e.g.*, 400 nm) will settle in the membrane pores within 50 seconds, the time necessary for a AuNP to migrate from conjugate pad to test zone. Therefore, further increasing particle size will decrease AuNP capture and thus the sensitivity of LFA because larger AuNPs have slower diffusion rates.

These examples demonstrate the importance of size control in AuNP-based IVD technologies. In fact, the profound impact of particle size on IVDs was also observed in a number of other noblemetal nanostructures. For instance, for Ag nanoparticle-based surface-enhanced Raman scattering (SERS) detection, the optimal size of Ag nanoparticles for providing a maximum SERS signal of adsorbed R6G was found to be ~50-60 nm. ¹³³ In a Pt nanoparticle-based colorimetric assay, among Pt nanoparticles with diameters in the range of 50-280 nm, ~150 nm Pt nanoparticles gave the highest signal intensity. ⁵⁸

3. Impact of Shape

3.1. Control of Shape

In recent years, a number of approaches have been reported to achieve shape control in seeded growth. Here we highlight a couple of representative examples that can effectively and tightly control the shape with relatively clear mechanistic understanding. While following discussions may be applied to all types of seeds, we will focus on the growth of single-crystal seeds coved by a set of low-index facets, including {111}, {100} and {110}, as a model system.

Facet-specific capping is an effective approach to control the shape of noble-metal nanocrystals. A7, 106 This approach relies on the introduction of a facet-specific capping agent to a synthesis, which can preferentially bind to specific type of facet of a growing seed. It is considered a thermodynamic approach because a capping agent reduces the surface free energy (γ) of a specific facet through chemisorption. For a noble-metal nanocrystal with a face-centered-cubic (fcc) crystal structure, the surface free energies of low-index facets increase in the order of $\gamma_{\{111\}} < \gamma_{\{100\}} < \gamma_{\{110\}}$. Therefore, the most thermodynamically stable shape for a noble-metal nanocrystal is truncated octahedron covered by $\{111\}$ and $\{100\}$ facets (see Figure 4A) as this shape ensures a minimal surface free energy. When a reaction is dominated by thermodynamic

control, seeded growth will proceed along the pathway that minimizes the total surface free energy of the system. Therefore, in the absence of any facet-specific capping agent, the growth of a truncated octahedral seed will likely produce larger sized truncated octahedron without change in shape, just like the case shown in Figure 1C. In the presence of a capping agent, however, the truncated octahedral shape can be changed remarkably.⁴⁷ As shown in Figure 4A, a {100}-specific capping agent can passivate (100) surface and lower $\gamma_{\{100\}}$. Therefore, the growth of a truncated octahedral seed is directed to preferentially occur along the <111> directions, resulting in the formation of cuboctahedron and then cube. On the contrary, a {111}-specific capping agent can block (111) surface and induce growth towards the <100> directions, leading to the formation of octahedron as the final product. Over the past, a large number of effective capping agents for different types of facets have been reported. Notable examples include PVP and Br for $Ag\{100\}$, $^{106, 135}$ citrate for $Ag\{111\}$; 106 Br^- and I^- for $Pd\{100\}$, 136 HCHO and CO for $Pd\{111\}$; 137 , ¹³⁸ Br⁻ and CO for Pt{100}. ^{96, 139, 140} Although the explicit mechanism responsible for the specificity of a capping agent is still unclear, some studies indicate that good match in geometry between the capping agent molecule and metal surface plays a key role in ensuring the specificity. 141-143

Kinetic control through manipulating the rates of atom deposition and surface diffusion is another effective approach to control the shape evolution during a seeded growth.⁴⁷ Using truncated cube with six side faces being blocked by capping agents as a model seed, Figure 4B illustrates how the ratio between the rates of atom deposition and surface diffusion ($V_{\rm dept}/V_{\rm diff}$.) affect the growth pathway of a seed and thus control the shape.¹⁴⁴ In this model, newly formed atoms from the reduction of a precursor are expected to deposit on the corners of a cubic seed and migrate to edges and side faces through surface diffusion because corners are more active than other sites. In an extreme case, when $V_{\rm dept}/V_{\rm diff}$. >> 1, most adatoms will stay at the corners of a cubic seed, resulting in the formation of an octapod as final product. In another extreme ($V_{\rm dept}/V_{\rm diff}$. << 1), the adatoms at corners will migrate to edges and side faces, promoting the formation of a cuboctahedron. Nanostructures of other shapes (e.g., concave cube and truncated cube) will form when $V_{\rm dept}/V_{\rm diff}$ is in between the two extremes. These expectations in the model were validated by experiments (e.g., growth of Pd cubic seeds; see the electron microscope images in Figure 4B), where $V_{\rm dept}$ and $V_{\rm diff}$ were separately and tightly controlled with an experimental setup (see Figure 1A). Specifically, $V_{\rm dept}$ can be controlled by adjusting the injection rate of a syringe pump, with

which metal precursor is added to the reaction solution. $V_{\text{diff.}}$ on the other hand can be varied by a temperature controller as diffusion is a thermally driven process. This powerful approach is applicable in many types of metals and seeds, ranging from monometallic systems to bimetallic systems; ¹⁴⁵⁻¹⁴⁷ and from single-crystal seeds to twin defects-contained seeds. ¹⁴⁸

It is worth mentioning that, under certain strict conditions, the growth of a seed with a highly symmetric shape can be induced towards an unsymmetric pattern. This case generally happens when: *i*) atom supply is low enough so the amount of atoms is only sufficient to nucleate on limited sites of seed surface; and *ii*) the energy barrier to surface diffusion is sufficiently high so the adatoms will not spread across the seed surface.⁴⁷ For example, the growth towards one of six {100}-covered side faces of a cubic seed results in the formation of a pencil-like nanostructure (Figure 4C).¹⁴⁹ Such an unsymmetric growth can be more dynamic by coupling with a facet-specific capping agent. For instance, one-dimensional bars will be obtained with the assistance of a {100}-specific capping agent. Other examples that involves different types of seeds and unsymmetric growth patterns can be found in recent publications.¹⁵⁰⁻¹⁵³

3.2. Shape-controlled Nanostructures in IVDs

Compared to size control, shape control is even more effective and versatile in enhancing the properties of a noble-metal nanostructure and thus its performance in IVDs. For instance, the LSPR peak of a Au or Ag nanostructure is more sensitive to its shape relative to size.^{77, 117} Steric effect in interaction with biomolecules caused by the increase of particle size can be minimized in the case of shape control. Moreover, shape control is more cost-efficient since it avoids the increase of materials usage.

In the SPR biosensor (see a model in Figure 2A), for example, the signal enhancement and detection sensitivity have a strong dependence on the shape of Au nanostructures as enhancers. Kwon *et al.* studied the shape effect in SPR biosensor by comparing the performance of Au nanostructures with quasi-spherical and rod-like shapes (Figure 5A, B). Both Au nanostructures possess at least one dimension in the 40-50 nm range. Thrombin was chosen as a model biomarker, which was captured by the DNA aptamer probe attached to the SPR-chip surface and the specific antibody conjugated on the Au nanostructures to form a sandwich complex during an assay. As shown by the spectra in Figure 5A, B, the major LSPR peaks for the Au quasi-spherical nanoparticles and nanorods were located at ~640 nm and ~530 nm, respectively. This difference in LSPR peak can be ascribed to the difference in particle shape. Under the same assay conditions,

the minimum thrombin concentrations detected by the Au quasi-spherical nanoparticles and nanorods were 1 and 10 aM, respectively, (see Figure 5C, D). This difference in signal generation and thus detection sensitivity originated from the changes in the real and imaginary components of the refractive index of the film at the chip-solution interface that were induced by the adsorbed Au nanostructures. The poorer detection performance of the Au nanorods relative to the Au quasi-spherical nanoparticles could be ascribed to that fact that: *i*) the nanorods induced a smaller change in the real component of the refractive index, since the volume of the nanorods is ~3-fold lower than that of the quasi-spherical nanoparticles with the same particle number; and *ii*) near-field plasmonic coupling occurred in the case of nanorods due to the overlap between particle LSRP profile and the wavelength of light source in the sensor device (760 nm), which affected the imaginary component of the refractive index. The shape-dependent performance of SPR biosensor was extensively investigated in other studies, where Au nanostructures with various shapes were examined. ¹⁵⁵⁻¹⁵⁷

SERS is of great interest for IVDs because of its high sensitivity, specificity, and multiplexing capabilities. 158-160 In SERS, the electric fields (E-fields) of a plasmonic nanostructure (i.e., SERS substrate) can enhance the Raman signal of molecules in their vicinity by a factor of E^4 . In general, SERS is applied to IVD tests in two ways – capturing and identifying analytes in a sample directly by a substrate; and using SERS "tags" that were prepared by coating substrates with probe molecules of known Raman fingerprints. In either way, the SERS enhancement factor (EF) of a substrate largely determines the sensitivity of SRES detection. At those regions of a substrate with drastically intensified E-field (so-called "hot spot"), Raman signal can be enhanced by many orders of magnitude (up to $\sim 10^{14}$), enabling single-molecule detection. ^{161, 162} Therefore, in SERS detection, much attention has been paid to develop SERS substrates with strong and reproducible hot spots. Shape plays a critical role in determining the number and strength of hot spots on a substrate and thus the EF. Both experimental and simulation results have demonstrated that hot spots oftentimes locate at the tips of a nanoscale substrate with sharp features (e.g., corners and edges). 161, 163 For example, Ag nanocube with sharp corners and edges provides a much higher EF compared to Ag nanosphere with the similar dimension (see Figure 6A). 164 This difference in EF is more evident (10⁸ for Ag nanocube versus 10⁶ for Ag nanosphere) when the nanoparticle is deposited on a Au or Ag film, which can couple with the LSPR of the nanoparticle and significantly enhance its E-fields.

An effective approach to boost the EF of a nanostructure is to create as many tips on its surface. 165-167 In a recent theoretical study based on Finite-Difference Time-Domain (FDTD) simulations, the EF of Au nanoshells with a number of spikes on the surface was calculated to be several orders of magnitude greater than that of Au nanoshells with a smooth surface (Figure 6B). 168 Significantly, the EF of such spiky nanoshells was demonstrated to be sensitive to the subtle change of surface geometry. For example, the EF of an ordered spiky nanoshell with identical spikes placed symmetrically (spike height of 58 nm, tip radius of 5 nm, and cone angle of 60°) was up to ~10 times smaller than that of a disordered spiky nanoshell with random spikes (spike heights between 50-65 nm, tip radii between 2-6 nm, and cone angles of 30-75°). In addition, the EF was quite sensitive to the heights of spikes. Under 784 nm laser excitation, the EFs of disordered spiky nanoshells with short (38-53 nm), medium (50-65 nm), and long (58-73 nm) spikes were at the levels of ~10², ~10³, and ~10⁵, respectively. In a recent applied research, Au nanostars with multiple spikes on the surface were utilized as sensitive SERS substrate for multiplexed detection of Zika virus (ZIKV) and dengue virus (DENV) through the platform of lateral flow assay (Figure 6C). 169 Specifically, two types of SERS tags were prepared by sequentially functionalizing Au nanostars with two probe molecules with different Raman fingerprints and antibodies specific to ZIKV and DENV, respectively. The SERS tags allowed for sensitive detection of both Zika and dengue virus in the same test line.

In recent years, artificial enzymes (or enzyme mimics) made of noble-metal nanostructures have emerged as a new type of functional materials for IVDs. $^{170-173}$ In a typical IVD test, the enzyme mimics are conjugated to bioreceptors and specifically generate detection signal by catalyzing enzyme substrates. Compared to their natural counterparts, enzyme mimics are more stable owing to the excellent stabilities of noble metals. In this niche filed, the major challenge is to enhance the catalytic efficiency of mimics since it largely determines the intensity of detection signal and thus the assay sensitivity. It has been demonstrated that the catalytic efficiency of an enzyme mimic has a strong dependence on the arrangement of atoms on the surface, which is correlated to the geometric shape of the mimic. For example, the catalase-like activity (*i.e.*, decomposition of H_2O_2 into O_2) of $\{111\}$ -covered Pd octahedrons was measured to be much higher than that of $\{100\}$ -covered Pd nanocubes under the same conditions (Figure 7A). 174 As revealed by theoretical simulations, this difference in catalytic activity can be ascribed to the difference in reaction energy (E_r) of the rate-limiting step (E_r = -2.81 for Pd $\{111\}$ versus E_r = -2.64 for Pd $\{100\}$).

It is worth noting that the catalase-like activity of noble-metal nanostructures enables the translation of molecular recognition events into easily measurable physical parameters such as volume and pressure of oxygen gas. Based on these signal-transducer principles, simple and sensitive point-of-care IVD tests were established.^{175, 176} In a recent work by Gao *et al.* (Figure 7B),¹⁷⁷ Pt concave nanocubes encased by high index facets were demonstrated to possess a peroxidase-like activity that was ~1,500- and 4-times higher than those of natural peroxidases and Pt nanospheres, respectively. The peroxidase-like property of Pt concave cubes allowed them to generate an intense color signal by catalyzing chromogenic substrates. Using colorimetric enzymelinked immunosorbent assay (ELISA¹⁷⁸⁻¹⁸⁰) as a model IVD platform, antibodies conjugated Pt concave nanocubes as labels were able to detect prostate-specific antigen (PSA, a biomarker of prostate cancer) with a broad linear range (20-2,000 pg/mL) and a detection limit of 0.8 pg/mL, which is much lower than that of commercial ELISA kit.

Besides those abovementioned examples, shape of a noble-metal nanostructure also affects the generation of other types of detection signal in IVDs. For instance, in metal-enhanced fluorescence (MEF), the enhancement of fluorescence signal has a strong dependence on the plasmonic properties that are largely determined by the shape of a nanostructure. ^{181, 182} The color of a Au or Ag nanostructure suspension can be tuned by changing the particle shape, which allows for multiplexed detection of biomarker/virus with colorimetric assays. ¹⁸³ Electrochemical signal of a noble-metal nanostructure can also be enhanced by carefully controlling the shape. ^{184, 185}

4. Impact of Elemental Composition

4.1. Control of Elemental Composition

Elemental compositions and their spatial distributions of a noble-metal nanostructure can be conveniently controlled *via* seeded growth. Here we use bimetallic nanostructure as a model system to illustrate the control of elemental composition. The principles and synthetic strategies presented here can be extended to multi-metallic systems.

Figure 8A shows the three possible growth modes that may involve in the deposition of metal N on the surface of a seed made of metal M. In thermodynamics, the growth mode is determined by the surface energies of three interfaces – $\gamma_{m/s}$ for the seed and solution, $\gamma_{n/s}$ for the deposited layer and solution, and $\gamma_{m/n}$ for the deposited layer and seed. The values of these surface energies are determined by a number of parameters such as bonding energy, type of solution, lattice

mismatch, and crystallinity. Depending on the relationship between these surface energy terms, three types of growth modes are expected: Frank-van der Merwe (FM) or layer-by-layer, Volmer–Weber (VW) or 3D island, and Stranski–Krastanov (SK) or mixed modes (Figure 8A). 107, 186 Nevertheless, the situations presented in Figure 8A only describe the ideal conditions when the system is solely under thermodynamic control. In practice, however, the growth of a seed is oftentimes governed by a combination of thermodynamic and kinetic parameters. When the kinetics is able to inhibit the system from reaching thermodynamic equilibrium, the growth mode will be influenced by kinetic control. For example, the 3D island mode can be switched to the mixed mode or even layer-by-layer mode when the rate of surface diffusion is adjusted to be sufficiently larger than that of atom deposition (see Figure 4B), and vice versa.

Using truncated cubic seed and layer-by-layer growth mode as a model example, Figure 8B shows the capability of seeded growth in controlling the elemental distribution of bimetallic nanostructures. In this model, we assume that the seed surface is not absorbed with any capping agents. Therefore, atom deposition is expected to preferentially occur on the six side faces of a seed because of their relatively high surface free energy. Three representative types of bimetallic nanostructures with different elemental distributions can be obtained: *i*) M@N core@shell nanostructures; *ii*) M-N hybrid nanostructures with both M and N exposing on the surface; and *iii*) M@M/N nanostructures with a shell of M/N alloy on the surface.

In the case of M@N nanostructures, newly formed atoms are required to be added to the entire surface of a seed in order to form a conformal shell. To achieve such a conformal coating, an effective strategy is to accelerate surface diffusion during the synthesis to force the adatoms to spread across the entire surface of a seed. It should be noted that the shell thickness in an M@N nanostructure can be precisely controlled at the atomic level by simply adjusting the amount of metal precursors. Examples could be found in recent publications. As discussed in Section 3.1, in principle, M-N hybrid nanostructures are formed when the atom supply is low enough and the energy barrier to surface diffusion is sufficiently high. M@M/N nanostructures can be synthesized through co-reduction of precursors to M and N. M@M/N nanostructures of M and N in the alloy shell can be conveniently controlled by adjusting the molar ratio of the two precursors. Alternatively, the M/N alloy shell can be formed through galvanic replacement between metal M and precursor of metal N (see Section 5.2 for more details about galvanic replacement).

It should be mentioned that bimetallic nanostructures with more sophisticated elemental

distributions can be synthesized by varying the conditions presented in Figure 8B. For example, M@N@M@N nanostructures with alternating shells can be obtained by sequentially adding precursors to N and M.¹⁹⁰ By carefully manipulating the reaction kinetics, M-N hybrid nanostructures with different proportions of M and N exposing on the surface can be obtained. Moreover, through the combinations and permutations of the cases shown in Figure 8A and B, it is possible to prepare multi-metallic nanostructures with diverse elemental compositions and distributions.

4.2. Elemental Composition-controlled Nanostructures in IVDs

In general, noble metals can be classified into two major categories – the coinage metals (*i.e.*, Au and Ag) and the platinum-group metals (*i.e.*, Pd, Pt, Rh, Ir, and Ru).¹⁹¹ Nanostructures of coinage metals possess tunable SPR properties in a broad range of wavelengths, but have limited use in catalysis. In contrast, nanostructures of platinum-group metals are highly active in catalysis, but do not display remarkable SPR properties.¹⁹¹ It should be emphasized that certain properties of noble-metal nanostructures within a category could be distinctively different because the inherent nature of metal is unique with each other. For example, the plasmonic sensitivity of Ag nanorods is up to 2 times higher than that of Au nanorods with similar resonance wavelengths.¹⁹² The catalytic activity of Pt nanocubes as artificial enzymes is ~10 times higher than that of Pd nanocubes with the same size.^{193, 194} Apparently, elemental composition of a noble-metal nanostructure plays an important role in determining its properties and performance in IVDs.

In following discussion, instead of monometallic system, we will use bimetallic system to demonstrate that the performance of a noble-metal nanostructure in IVDs can be substantially improved by incorporating a second metal. In many cases, a subtle change in elemental composition makes a dramatic difference. The ideas and strategies discussed below can be extended to multi-metallic systems.

Firstly, a second metal can enhance the detection signal generated from a nanostructure. For example, peroxidase mimics made of inorganic nanomaterials have received great interest as emerging artificial enzymes for colorimetric IVDs.¹⁷¹ While various peroxidase mimics have been actively developed in recent years, their efficiencies in terms of catalytic constant (K_{cat} , which measures the maximum number of color products yielded from a catalytic reaction per second per enzyme or mimic) have not been substantially improved. K_{cat} of most reported peroxidase mimics with sizes 1-100 nm is limited to 10^4 s⁻¹, which is only up to one order of magnitude greater than

that of horseradish peroxidase (HRP, $K_{\text{cat}} = 10^3 \text{ s}^{-1}$) as the natural counterpart. Such a limitation in catalytic efficiency forms the bottleneck in improving the detection sensitivity of relevant IVD tests. In a recent study, our research group has developed a novel type of peroxidase mimic – Pd@Ir_{1-2L} core@shell nanocubes (Figure 9A) – that was prepared by coating ~18 nm Pd nanocubes with a few atomic layers of Ir. 194 The Pd@Ir_{1-2L} cubes displayed a record-high catalytic efficiency with a K_{cat} at the level of 10^6 s^{-1} , which is approximately 2 and 3 orders of magnitudes higher than those of the initial Pd nanocubes and HRP, respectively (Figure 9B). Obviously, the enhanced efficiency of Pd@Ir_{1-2L} cubes relative to the Pd nanocubes as the seeds can be attributed to the coat of Ir shells. To understand the impact of Ir shells on the catalytic efficiency, a set of Pd@Ir cubes with different molar ratios of Ir to Pd were prepared and their K_{cat} values were determined. Interestingly, it was found that the K_{cat} values showed a volcano-shaped dependence on the Ir contents, with a maximum point corresponding to approximately a monolayer of Ir on Pd surface. Density functional theory (DFT) based theoretical calculations were conducted to gain more insights into the experimental observations, where Pd(100), Ir(100), Ir_{1L}/Pd(100), and Ir_{3L}/Pd(100) were compared. The simulation results indicated that Ir_{1L}/Pd(100) among the four surfaces was the most reactive since the adsorption energies of key species in the catalytic reaction on this surface were most exothermic, which agreed well with the experimental results. Using ELISA as a model IVD platform and PSA as a disease biomarker, the Pd@Ir_{1-2L} cube-based ELISA achieved a detection limit of 0.67 pg/mL, which is ~110-fold lower than that of the conventional HRP-based ELISA (Figure 9C, D). This substantial improvement in detection sensitivity can be ascribed to the enhanced catalytic efficiency of Pd@Ir_{1-2L} cubes relative to HRP because all the antibodies and materials used in the two ELISAs were kept the same. Enhancing the detection signal by incorporating a second metal is also evident in electrochemical biosensors. 195, 196

Secondly, a second metal can endow a nanostructure with dual functionalities. For instance, in a recent work, we coated conventional AuNPs of ~40 nm in diameter with conformal, thin skins of Pt to form a unique type of nanostructure – Au@Pt_{nL} core@shell NPs (*n*L: *n* atomic layers of Pt, Figure 10A). Here *n* could be conveniently and precisely controlled in the range of 1-10 by adjusting the amount of Pt precursor introduced to the growth of AuNP seeds. It was found that the plasmonic activity of the AuNP cores in the Au@Pt_{nL} NPs could be well retained as long as the Pt shell was ultrathin (several atomic layers). Therefore, similar to conventional AuNPs, the Au@Pt_{nL} NPs would display a distinct red color. On the other hand, the Pt shells on the surface

endow the Au@Pt_{nL} NPs with high peroxidase-like activities, allowing them to generate intense blue colored products by catalyzing the oxidation of 3,3',5,5'-tetramethylbenzidine (TMB, a typical peroxidase substrate 198) by H_2O_2 in aqueous solution. The catalytic efficiency, in terms of K_{cat} , of $Au@Pt_{nL}$ NPs increased rapidly as n increased and became saturated at n = 4. Note the initial AuNPs almost have no peroxidase-like activities. Significantly, the intensity of blue color from catalysis is much stronger than that of the intrinsic red color from plasmonics. Taking Au@Pt4L NPs as an example (Figure 10B), the molar extinction coefficient of NPs themselves was determined to be ~9.5×10⁹ M⁻¹ cm⁻¹. In contrast, the equivalent molar extinction coefficient of the blue colored molecules from catalysis was determined to be $\sim 1.8 \times 10^{13}~M^{-1}~cm^{-1}$. The dual functionalities – plasmonics and catalysis – of the Au@Pt_{nL} NPs make them extremely suitable for colorimetric lateral flow assay (LFA). They can offer two different colorimetric signals (Figure 10C): one red color generated by the plasmonic AuNP cores (low-sensitivity mode) and the other more sensitive blue color produced by the catalytic Pt shells (high-sensitivity mode), achieving an "on-demand" tuning of the detection performance. In practice, the low-sensitivity mode is first performed. High-sensitivity mode is only needed when weak or no signal is observed under lowsensitivity mode (e.g., samples with low concentrations of analytes). Figure 10D shows the results of LFAs for PSA standards using the Au@Pt4L NPs and conventional AuNPs as labels. Under lowsensitivity mode, the detection limit of Au@Pt4L NP-based LFA is similar to that of conventional AuNP-based LFA (2 ng/mL PSA). Under high-sensitivity mode, PSA with concentrations as low as 20 pg/mL could be detected, rivalling the sensitivity of more sophisticated IVD technologies such as ELISA. Such a significant enhancement in sensitivity for LFA (two orders of magnitudes) is only paid by a simple, 5-minute substrate treatment process at room temperature. It is worth noting that similar concept of dual functionalities achieved by bimetallic systems has been actively explored in more recent studies.^{58, 199}

Moreover, a second metal can enhance the stability of a nanostructure, ensuring reliable IVDs. Nanostructures of Ag are known to possess the strongest plasmonic activities among noble metals owing to their appropriate electronic structure and thus dielectric function. 77, 200-202 Nevertheless, the excellent plasmonic properties of Ag nanostructures have not been fully utilized in IVDs and many other applications due to the relatively poor chemical and structural stabilities of Ag under unfavorable environments. Therefore, development of approaches that can stabilize Ag nanostructures without compromising their plasmonic properties is critical to the practical

applications of Ag nanostructures. An effective approach is to incorporate Ag nanostructures with Au, which is much more stable and has almost the same lattice constant as Ag. For example, Yang et al. reported a robust synthesis of Ag@Au core@shell nanocubes by depositing Au atoms onto Ag nanocubes.²⁰⁶ The key to the successful synthesis relied on the inhibition of galvanic replacement (see Section 5.2 for details) between Ag and Au³⁺ by introducing a strong reducing agent to rapidly consume Au³⁺ ions. The conformal and ultrathin Au shells (sub-10 atomic layers, see a representative sample in Figure 11A) were able to protect the Ag nanocubes in oxidative environments. The Ag@Au nanocubes displayed surface plasmonic properties essentially identical to those of the initial Ag nanocubes. Significantly, because of the stronger adsorption of Raman probe molecules on Au surface relative to Ag, the Ag@Au nanocubes exhibited an outstanding and stable SERS activity with an enhancement factor ~5-fold greater than that of Ag nanocubes (Figure 11B). In another study by Gao et al., 207 instead of core@shell structure, Au was mixed with Ag to form a Ag/Au alloyed structure (Figure 11C). Unlike conventional methods based on co-reduction of Au and Ag precursors, the Ag/Au alloy was formed through annealing process at elevated temperatures (~1,000 °C). The high-temperature annealing promoted the complete mixing of Ag and Au at the atomic scale. The alloyed nanostructure obtained from this method is featured by homogeneous distribution of Ag and Au, minimal crystallographic defects, and the absence of structural and compositional interfaces. These features ensured outstanding plasmonic properties (e.g., large extinction cross sections and narrow bandwidths) and enhanced stabilities for the resultant Ag/Au alloyed nanostructures (see Figure 11D). Collectively, these approaches preserved the superior plasmonic properties of Ag while adopted the excellent stabilities of Au, making the Au-incorporated Ag nanostructures particularly suitable for IVDs (e.g., SPR and SERS biosensing).

5. Impact of Internal Structure

5.1. Control of Crystallinity

Most noble metals crystallize in the face-centered cubic (fcc) lattice, with a characteristic stacking sequence of ABCABC along the closely packed <111> direction.⁴⁹ However, planar defects can be involved during nanocrystal growth, disrupting the stacking sequence. The two most common types of planar defects observed in fcc metal nanocrystals are twin boundary and stacking fault. In general, a twin boundary ("||") separates two crystal domains and creates a mirror image

(e.g., ABC||CBA). Stacking fault ("[]") is formed when a layer in the natural stacking sequence is missing (e.g., ABC[]BC) or an additional layer is added to the sequence (e.g., ABC[B]ABC). Depending on the type and number of planar defects involved, noble-metal nanostructures can be classified into four major categories: single-crystal (no defect), singly twinned (one twin boundary), multiply twinned (more than one twin boundaries), and stacking-fault-contained structures. Representative example of each category is shown in Figure 12A. 148, 208, 209 It should be emphasized that planar defects are typically introduced into crystal lattice as early as the homogeneous nucleation stage in a one-pot synthesis. Once the nuclei have evolved into seeds, their crystallinities in terms of planar defects are usually maintained during the later on crystal growth process. In this regard, it is challenging to intentionally control the planar defects involved in a metal nanostructure due to the lack of clear mechanistic understanding on nucleation process and the shortage of analytical tools capable of analyzing the evolution from atoms to nuclei and seeds. Nevertheless, in some case studies, nanostructures with desired crystallinities can be synthesized in high purity by carefully controlling the reaction conditions. For example, oxidative etching was demonstrated to be an effective approach to selectively remove Ag or Pd seeds with twin defects. 148, 210-212 Pd nanostructures with a specific planar defect can be obtained by controlling the initial reduction rate of a precursor in a polyol synthesis.²⁰⁹ Future advancement in instrumentation and quantitative understanding on pathways of nucleation and growth will enable us to better control the planar defects for noble-metal nanostructures.

It is worth noting that, in addition to the introduction of planar defects, the crystallinity of noble-metal nanostructures can be changed by altering the inherent crystal structure. In recent years, a number of noble-metal nanostructures with unusual crystal structures have been reported. Representative examples include Au and Rh nanosheets with an *hcp* structure, ^{213, 214} Ag nanowires with a 4H or 2H structure, ^{215, 216} Pd nanocubes with an *fct* structure, ²¹⁷ and Ru nanostructures with an *fcc* structure. ¹⁴⁶ These nanostructures with unique crystallinities can be obtained through chemical synthesis or post-treatment. More details and insights regarding this topic can found in a recently published review article. ²¹⁸

5.2. Control of Hollowness

Noble-metal nanostructures with hollow interiors have received great interest in recent years because of the unique and useful properties that can't be offered by their solid counterparts.²¹⁹ A number of approaches have been developed to produce hollow nanostructures, including those

based on templating synthesis,^{220, 221} selective etching,^{222, 223} Ostwald ripening,^{224, 225} galvanic replacement,^{226, 227} and Kirkendall effect^{228, 229}. Herein, we briefly introduce galvanic replacement as a simple yet effective approach to generate hollow nanostructures and highlight some recent developments.

Galvanic replacement is essentially an electrochemical process, involving the oxidation/dissolution of a metal template by the ions of another metal having a higher reduction potential. When metal nanocrystals are used as the templates, hollow nanostructures with tunable degrees of hollowness can be synthesized *via* galvanic replacement reaction. In general, galvanic replacement tends to start from the sites of a nanoscale template with the highest surface free energy, whereas the newly formed atoms are deposited on the remaining sites. Size, 232, 233 Using a truncated nanocube of metal M with side faces being covered by capping agents as a model template, Figure 12B illustrates the morphological and compositional changes at different stages of a galvanic replacement reaction: $M + N^{y+} \rightarrow M^{x+} + N$ (not balanced, for simplicity). In brief, metal M is dissolute from the corners of a cubic template because of their high energy relative to side faces (which are passivated by capping agents). Meanwhile, atoms of metal N are deposited on side faces to form M/N alloy on the surface. Continuous dissolution of M from the interior of template results in the formation of hollow nanostructures.

This method is featured by simplicity and versatility. Galvanic replacement is a simple reaction that is limited by no more than the requirement of an appropriate difference in reduction potentials of the two metals. The extent of hollowness can be conveniently controlled by varying the amount of precursor introduced to the reaction solution. The size and shape of the hollow nanostructures can be controlled by using nanocrystals with specific morphologies as the templates. Elemental compositions of the final nanostructures can be tuned by using different types/amounts of salt precursors. Moreover, by coupling with other mechanisms, hollow nanostructures with more delicate features can be obtained. For example, Ag/Au or Ag/Pd hollow nanostructures with controllable elemental compositions were synthesized by coupling galvanic replacement with Kirkendall effect.²³⁴ In a recent work, Au nanoboxes with ultrathin walls (<10 atomic layers) were obtained by integrating site-selective passivation and chemical etching into galvanic replacement.²³⁵ It should be mentioned that galvanic replacement also has some drawbacks to consider. For instance, metals with high reduction potentials (*e.g.*, Au and Pt) can barely serve as templates. For a specific template, the wall thickness and composition of final hollow

nanostructures are largely confined by the stoichiometry of galvanic reaction.

5.3. Internal Structure-controlled Nanostructures in IVDs

To the best of our knowledge, IVD platforms relied on the unique properties of planar defects of noble-metal nanostructures have not been reported in literature so far. Therefore, in this section, we will focus on the influences of hollowness on the performance of a noble-metal nanostructure in IVD applications.

Hollow nanostructures of Au or Ag are known to have better plasmonic properties compared to their solid counterparts thanks to the interaction of plasmon fields in the inner and outer layers, in compliance with the plasmon hybridization mechanism. ²³⁶ The hybridizations of the plasmons leads to the enhanced plasmon fields together with homogeneous distribution and red-shift of plasmon resonances.²³⁷⁻²³⁹ In a recent work, Genç et al. systematically investigated the plasmon resonances of Au/Ag cubic nanostructures with different extent of hollowness (including solid nanocubes, nanocubes with pinholes, nanoboxes with completely hollow interior, and nanoframes with an open structure) at the nanoscale.²⁴⁰ Electron energy loss spectroscopy (EELS) was employed to obtain the spatially resolved mapping of plasmon resonances. Among those nanostructures, nanoboxes exhibited homogeneous distribution of plasmon resonances. As shown by the selected area EEL spectra obtained from different sites of a single nanobox (Figure 13A), the plasmon peaks were located in a relatively narrow range of ~2-2.5 eV and had similar energies as one another. The abundance maps clearly show the homogeneous distribution of plasmon resonance all around the nanobox. These experimental observations were accurately correlated with the simulation results based on the boundary element method (BEM²⁴¹). In contrast, other nanostructures showed much less homogeneous distributions. This work revealed that the homogeneous distribution of plasmon resonances is the key feature for the enhanced plasmonic properties of hollow nanostructures. As a proof-of-concept demonstration, the nanoboxes were applied to label free SPR detection of bovine serum albumin (BSA) and anti-BSA antibodies, of which performance was benchmarked against solid Au nanoparticles (see Figure 13B). The adsorption of biomolecules on the plasmonic nanostructures induces refractive index changes that can be measured by a UV-vis spectrometer. Compared with solid Au nanoparticles, ~4× stronger shifts in extinction wavelength was observed for the Au/Ag nanoboxes. This enhanced detection sensitivity could be ascribed to the enhancement of localized electromagnetic field around the hollow nanoboxes that allowed for sensitive responses to binding events in their vicinity.

The hollow feature of a nanostructure also benefits its SERS enhancement and thus SERS biosensing. For example, in a work by Lim *et al.*,²⁴² gold nanobridged nanogap particles (Au-NNPs, see Figure 13C) with ~1 nm gap between the core and shell were synthesized using dyed DNAs-functionalized Au nanoparticles as the seeds. Owing to the drastically enhanced electromagnetic field localized in the interior-gap region of the Au-NNP, Raman signal from dyes trapped in the nanogap can be significantly amplified. Compared with solid Au nanoparticles, Raman signal from the Au-NNPs was approximately two orders of magnitude stronger. Atomic force microscope (AFM)-correlated nano-Raman measurement was performed to determine the enhancement factor (EF) of the Au-NNPs. Radom mapping of 200 individual Au-NNPs showed that their EF values were narrowly and uniformly distributed within the range of 1.0×10⁸ - 5.0×10⁹, making the Au-NNPs capable of single-molecule detection. Such a SERS enhancement by interior nanogap was also observed in Au/Ag double-walled nanoboxes.²⁴³ Notably, the size of nanogap was found to play an important role in determining the SERS EF. Overall, the EF continuously decreased as the gap size increased from ~1 to ~16 nm.

In addition to SPR and SERS, recent studies have demonstrated that hollow nanostructures can generate strong metal-enhanced fluorescence (MEF) and photoluminescence (PL). For instance, Au/Ag nanocages with major LSPR in the near-infrared (NIR) region were proven to be highly effective NIR-MEF substrates that are particularly suitable for biosensing.²⁴⁴ Au@Au/Ag core@shell nanostructure with controlled interior nanogaps could offer a highly intense PL signal that is ~30 and ~1,000 times stronger than those of solid Au nanoparticles and R6G as a typical organic fluorophore, respectively.²⁴⁵ Such enhanced PL intensity is mainly attributed to the plasmonic coupling between the core and shell, which results in a super-radiant plasmon mode and thereby an increased radiative damping rate.

It is worth noting that most of abovementioned enhanced performance relies on the superior plasmonic properties of hollow nanostructures. Nevertheless, hollow nanostructures have several other distinctive advantages over their solid counterparts that may be taken into consideration in future IVD development. For example, the outer and inner surfaces of a hollow nanostructure offer more flexibilities for biomolecule conjugation. The cavity in a hollow nanostructure affects its density/weight and thus transport properties (*e.g.*, diffusion and sedimentation),²⁴⁶ which may influence its performance in IVD tests. The enlarged surface area and active surface atoms of a hollow nanostructure can boost its catalytic activities, providing enhanced detection signal.^{75, 187}

6. Concluding Remarks

In this article, we have discussed recent progress on engineered noble-metal nanostructures for application in IVDs. Owing to their outstanding properties, excellent stabilities, and facile synthesis, noble-metal nanostructures have received ever increasing interest as signal transducers for IVDs over the past decade. In particular, thanks to the increased mechanistic understanding on nanocrystal growth and rapid advancement of characterization tools, one can now precisely tune the physical/chemical parameters (including size, shape, elemental composition, and internal structure) of a noble-metal nanostructure at the atomic level. Through careful control over these parameters, the physicochemical properties of a nanostructure can be optimized and therefore its performance in certain IVDs can be substantially enhanced. Effective methodologies for engineering noble-metal nanostructures have been introduced. The superior performance of engineered nanostructures with desired properties has been demonstrated in various IVD platforms, including those based on SPR, SERS, MEF, photothermal, photoluminescence, electrochemical, and colorimetric signal-transduction principles.

While not focused in this article, enhanced performance of noble-metal nanostructures in IVDs can also be achieved through approaches other than controlled synthesis of monodispersed nanocrystals. One effective approach is to carefully assemble nanoparticles to form nanoparticle aggregates with well-controlled spatial geometries. For instance, Lim et al. reported a type of highly SERS-active Au@Ag core@shell nanodumbbells (Figure 14A).²⁴⁷ The nanodumbbell was prepared by assembling two individual AuNPs by means of single-target-DNA hybridization followed by an overgrowth of Ag on the AuNP surfaces. SERS activity of the nanodumbbells was demonstrated to have a strong dependence on gap size between the Au@Ag nanoparticles and the Ag shell thickness. When Ag shell is ~5 nm and the two particles are in close contact (~0 nm), the SERS activity of the nanodumbbells is maximized with an EF at the level of 10^{12} that is sufficiently high for single-molecule detection. Xu et al. reported a smart design of AgNP aggregates with a pyramidal shape (Figure 14B).²⁴⁸ Briefly, DNA sequences embedded with disease biomarkerspecific aptamers were used to assemble Raman reporter molecules-labeled AgNPs to obtain the AgNP pyramids. The presence of biomarkers will shorten the gap distance between AgNPs in a pyramid because of the specific biorecognition by aptamers. As a result, the Raman signal of reporter molecules is greatly enhanced, allowing for attomolar biomarker detection. Significantly,

the AgNP pyramid is capable of multiplexed detection of biomarkers by embedding the DNA frames of the pyramid with multiple aptamers and modifying the AgNPs with different Raman reporter molecules. Another notable example is chiral assemblies of nanoparticles for plasmonic detection of biomarkers. As shown in Figure 14C, heterodimer of a AuNP and a AgNP can be formed through the antibody-antigen bridges.²⁴⁹ The constituent NPs with a prolate geometry (i.e., prolate ellipsoids) in a hereodimer are nonparallel to each other but have a distinct dihedral angle. Such dihedral angle results in the chiroplasmonic properties of the heterodimer. Therefore, the presence of biomarkers can be detected through the circular dichroism (CD) signal with a characteristic bisignated line shape. Apart from those nanoparticle aggregates at the nanometer scale, nanoparticle assemblies of larger sizes (e.g., micrometer scale) may also provide enhanced performance in IVDs. For instance, Kang et al. reported the self-assembly of ~10 nm AuNPs onto Au wire of ~15 μm in length in the presence of target DNAs.²⁵⁰ The resultant Au particle-on-wire structure was able to yield highly intense SERS signal owing to the formation of multiple SERS hot spots located at the junctions between AuNPs and Au wire, which enabled sensitive detection of pathogen DNAs. It is worth noting that the performance of particle aggregates in these examples may be further enhanced when the size, shape etc. of individual nanostructures are carefully controlled.

Taking advantage of the striking phenomena observed during nanocrystal growth is another effective approach to explore the applications of noble-metal nanostructures in IVDs. ²⁵¹ For instance, Rica *et al.* linked the biocatalytic activity of enzymes to the growth of AuNPs to obtain blue or red colored solutions in the presence or absence of the analyte, respectively (Figure 15A). ²⁵¹ In the absence of analyte, the reduction of Au³⁺ ions by H_2O_2 occurs at a fast rate, resulting in the formation of small-sized and well-dispersed AuNPs. The solution under these conditions is expected to display a red color. In the presence of an analyte, the enzyme catalase rapidly digests H_2O_2 , which slows down the kinetics of AuNP growth. As a result, larger sized AuNPs with irregular morphologies were formed. Consequently, the solution turns blue. This signal generation mechanism enables the detection of PSA in whole serum at the ultralow concentration of 1×10^{-18} g/mL. The concept of enzyme-guided nanocrystal growth for IVD tests was also demonstrated in the presence of pre-formed nanostructures as the seeds. ^{252, 253} For example, the growth of Ag on Au nanobipyramids with sharp tips can be controlled by enzyme alkaline phosphatase that generates 4-aminophenol as a reducing agent for Ag⁺ ions (Figure 15B). ²⁵² Au nanobipyramides

coated with different amount of Ag display diverse colors, which can be applied to sensitive detection of the H5N1 virus. Similarly, the growth pathway of Ag in the suspension of Au nanostars can be guided by enzyme glucose oxidase, which generates H₂O₂ that can reduce Ag⁺ ions.³⁶ As the reverse process of crystal growth, the phenomena associated with chemical etching of nanostructures can also be employed for IVD tests. For example, when Ag triangular nanoplates are etched by H₂O₂, the alternation of shape and size are accompanied by a substantial blue shift of the LSPR peak. This etching process can be linked to a biosensing system for DNA detection, where target DNA is labeled with glucose oxidase that generates H₂O₂ to etch Ag nanoplates (see Figure 15C).²⁵⁴

Coupling engineered noble-metal nanostructures with other types of functional materials for IVDs is a promising direction to explore. For instance, magnetic nanoparticles are widely used for easy separation and concentration of biomolecules owing to their responsive magnetic properties. Hybrid magnetic-metal nanostructures with multi-functionalities are expected to provide superior performance for IVD tests. A notable example is to use Fe₃O₄@Pt core@shell nanoparticles as labels for point-of-care tests, where Fe₃O₄ was responsible for enrichment of analytes from a sample while Pt as a catalyst could generate an intense color signal.⁵⁷ Two-dimensional nanomaterials (*e.g.*, MoS₂, ²⁵⁵ Bi₂Se₃, ²⁵⁶ graphene, ²⁵⁷ and graphene oxide²⁵⁸) can serve as supports to improve the properties of noble-metal nanostructures through the synergetic effects. For example, the enzymatic activity of AuNPs could be enhanced by graphene nanosheet as the support, making such hybrid catalysts extremely suitable for biosensing.²⁵⁷ In a recent study, nanosheets of NiCl₂ were demonstrated to be able to synergistically enhance the catalytic activities of Pd nanoparticles.²⁵⁹ These functional nanomaterials add a new dimension to the application of noble-metal nanostructures in IVDs.

Surface chemistry, especially chemical ligands on the surface, plays an important role in determining the performance of a noble-metal nanostructure in IVDs. Most metal nanostructures are synthesized in the presence of appropriate colloidal stabilizers and/or capping agents. ⁴⁹ As a result, the surfaces of as-synthesized nanostructures are oftentimes covered by chemical ligands through physical/chemical adsorptions. The surface ligands largely determine the charge, polarity, solubility, mobility, and activity of a nanostructure and thus affect its performance in IVDs. For example, in bioconjugation, metal nanostructures capped by negatively charged citrates can be readily modified with proteins through the electrostatic interactions. ²⁶⁰ In contrast, it is not

straightforward to achieve protein modification for those metal nanostructures capped by PVP as a neutral polymer. In plasmonics, surface ligand-free Au nanostars showed greatly enhanced refractive index sensitivity when compared with the PVP-capped counterparts, allowing for plasmonic biosensing with improved versatility and sensitivity.²⁶¹ In catalysis, the specific activities of Pt-group metal nanostructures are expected to be substantially enhanced when the surface ligands are removed.^{262, 263} Furthermore, post-functionalization of metal nanostructures with specific ligands (*e.g.*, thiol-terminated polyethylene glycol chains for bioconjugations⁵³ and amphiphilic block copolymers for self-assembly^{264, 265}) will facilitate their application in IVDs. Taken together, surface chemistry is an important aspect to be considered when applying a metal nanostructure to IVD tests.

Ultimately, we hope that the perspectives provided in this article can serve as a helpful resource for scientists in academia and industry who want to develop noble-metal nanostructures with desired properties for IVDs. In this emerging field, there are plenty of subjects deserve thorough exploration in the future. Our constantly refined mechanistic understanding and advanced experimental capabilities will enable us to produce engineered nanostructures at industrially relevant scales sought for development of simple, sensitive, and affordable IVD technologies.

Acknowledgments

This work was supported in part by the grants from the National Science Foundation (CHE 1834874 and CEBT 1804525), and the startup funds from University of Central Florida (UCF). Z. X. was partially supported by the UCF Preeminent Postdoctoral Program.

References

- (1) Turner, A. P.; Chen, B.; Piletsky, S. A. *In Vitro* Diagnostics in Diabetes: Meeting the Challenge. *Clin. Chem.* **1999**, *45*, 1596-1601.
- (2) Michalet, X.; Pinaud, F. F.; Bentolila, L. A.; Tsay, J. M.; Doose, S.; Li, J.; Sundaresan, G.; Wu, A. M.; Gambhir, S. S.; Weiss, S. Quantum Dots for Live Cells, *In Vivo* Imaging, and Diagnostics. *Science* **2005**, *307*, 538-544.

- (3) Khlebtsov, N.; Dykman, L. Biodistribution and Toxicity of Engineered Gold Nanoparticles: A Review of *In Vitro* and *In Vivo* Studies. *Chem. Soc. Rev.* **2011**, *40*, 1647-1671.
- (4) Jin, Z.; Hildebrandt, N. Semiconductor Quantum Dots for *In Vitro* Diagnostics and Cellular Imaging. *Trends Biotechnol.* **2012**, *30*, 394-403.
- (5) Rohr, U. P.; Binder, C.; Dieterle, T.; Giusti, F.; Messina, C. G.; Toerien, E.; Moch, H.; Schafer, H. H. The Value of *In Vitro* Diagnostic Testing in Medical Practice: A Status Report. *PLoS One* **2016**, *11*, e0149856.
- (6) Zhou, W.; Gao, X.; Liu, D.; Chen, X. Gold Nanoparticles for *In Vitro* Diagnostics. *Chem. Rev.* **2015**, *115*, 10575-10636.
- (7) Scott, M. G.; Bruns, D. E.; Boyd, J. C.; Sacks, D. B. Tight Glucose Control in the Intensive Care Unit: Are Glucose Meters up to the Task? *Clin. Chem.* **2009**, *55*, 18-20.
- (8) Peter, J. G.; Theron, G.; Dheda, K. Can Point-of-Care Urine LAM Strip Testing for Tuberculosis Add Value to Clinical Decision Making in Hospitalised HIV-Infected Persons? *Plos One* **2013**, *8*, e54875.
- (9) Gottlieb, S.; Woodcock, J. A Regulatory Perspective on *In Vitro* Diagnostics. *Nat. Biotechnol.* **2006**, *24*, 927-929.
- (10) Giljohann, D. A.; Mirkin, C. A. Drivers of Biodiagnostic Development. *Nature* **2009**, *462*, 461-464.
- (11) Ambrosi, A.; Airo, F.; Merkoci, A. Enhanced Gold Nanoparticle Based ELISA for a Breast Cancer Biomarker. *Anal. Chem.* **2010**, *82*, 1151-1156.
- (12) Beqa, L.; Fan, Z.; Singh, A. K.; Senapati, D.; Ray, P. C. Gold Nano-popcorn Attached SWCNT Hybrid Nanomaterial for Targeted Diagnosis and Photothermal Therapy of Human Breast Cancer Cells. *ACS Appl. Mater. Interfaces* **2011**, *3*, 3316-3324.
- (13) Rundle, A.; Neugut, A. I. Obesity and Screening PSA Levels Among Men Undergoing an Annual Physical Exam. *Prostate* **2008**, *68*, 373-380.
- (14) Thaxton, C. S.; Elghanian, R.; Thomas, A. D.; Stoeva, S. I.; Lee, J. S.; Smith, N. D.; Schaeffer, A. J.; Klocker, H.; Horninger, W.; Bartsch, G.; Mirkin, C. A. Nanoparticle-based Biobarcode Assay Redefines "Undetectable" PSA and Biochemical Recurrence After Radical Prostatectomy. *Proc. Natl. Acad. Sci. USA* **2009**, *106*, 18437-18442.
- (15) Rissin, D. M.; Kan, C. W.; Campbell, T. G.; Howes, S. C.; Fournier, D. R.; Song, L.; Piech, T.; Patel, P. P.; Chang, L.; Rivnak, A. J.; Ferrell, E. P.; Randall, J. D.; Provuncher, G. K.; Walt, D.

- R.; Duffy, D. C. Single-molecule Enzyme-linked Immunosorbent Assay Detects Serum Proteins at Subfemtomolar Concentrations. *Nat. Biotechnol.* **2010**, *28*, 595-599.
- (16) Asiago, V. M.; Alverado, L. Z.; Shanaiah, N.; Gowda, N. G.; Owusu-Sarfo, K.; Ballas, R.; Raftery, D. Early Detection of Recurrent Breast Cancer Using Metabolite Profiling. *Cancer Res.* **2010**, *70*, Abstract nr P3-10-18.
- (17) Turner, A. P. Biosensors: Sense and Sensibility. Chem. Soc. Rev. 2013, 42, 3184-3196.
- (18) Vashist, S. K.; Schneider, E. M.; Luong, J. H. Rapid Sandwich ELISA-based *In Vitro* Diagnostic Procedure for the Highly-sensitive Detection of Human Fetuin A. *Biosens. Bioelectron.* **2015**, *67*, 73-78.
- (19) Li, J.; Gao, Z.; Ye, H.; Wan, S.; Pierce, M.; Tang, D.; Xia, X. A Non-enzyme Cascade Amplification Strategy for Colorimetric Assay of Disease Biomarkers. *Chem. Commun.* **2017**, *53*, 9055-9058.
- (20) Jain, K. K. Nanotechnology in Clinical Laboratory Diagnostics. *Clin. Chim. Acta.* **2005**, *358*, 37-54.
- (21) Chi, X.; Huang, D.; Zhao, Z.; Zhou, Z.; Yin, Z.; Gao, J. Nanoprobes for *In Vitro* Diagnostics of Cancer and Infectious Diseases. *Biomaterials* **2012**, *33*, 189-206.
- (22) Cobley, C. M.; Chen, J.; Cho, E. C.; Wang, L. V.; Xia, Y. Gold Nanostructures: A Class of Multifunctional Materials for Biomedical Applications. *Chem. Soc. Rev.* **2011**, *40*, 44-56.
- (23) Rosi, N. L.; Mirkin, C. A. Nanostructures in Biodiagnostics. *Chem. Rev.* **2005**, *105*, 1547-1562.
- (24) West, J. L.; Halas, N. J. Engineered Nanomaterials for Biophotonics Applications: Improving Sensing, Imaging, and Therapeutics. *Annu. Rev. Biomed. Eng.* **2003**, *5*, 285-292.
- (25) Alivisatos, P. The Use of Nanocrystals in Biological Detection. *Nat. Biotechnol.* **2004**, *22*, 47-52.
- (26) Alvarez-Puebla, R. A.; Liz-Marzan, L. M. Traps and Cages for Universal SERS Detection. *Chem. Soc. Rev.* **2012**, *41*, 43-51.
- (27) Wang, C.; Daimon, H.; Onodera, T.; Koda, T.; Sun, S. A General Approach to the Size- and Shape-controlled Synthesis of Platinum Nanoparticles and Their Catalytic Reduction of Oxygen. *Angew. Chem., Int. Ed.* **2008**, *47*, 3588-3591.
- (28) Joo, S. H.; Park, J. Y.; Tsung, C. K.; Yamada, Y.; Yang, P.; Somorjai, G. A. Thermally Stable Pt/Mesoporous Silica Core-shell Nanocatalysts for High-temperature Reactions. *Nat. Mater.* **2009**,

- 8, 126-131.
- (29) Lee, I.; Delbecq, F.; Morales, R.; Albiter, M. A.; Zaera, F. Tuning Selectivity in Catalysis by Controlling Particle Shape. *Nat. Mater.* **2009**, *8*, 132-138.
- (30) Jain, P. K.; Huang, X.; El-Sayed, I. H.; El-Sayed, M. A. Noble Metals on the Nanoscale: Optical and Photothermal Properties and Some Applications in Imaging, Sensing, Biology, and Medicine. *Acc. Chem. Res.* **2008**, *41*, 1578-1586.
- (31) Sepulveda, B.; Angelome, P. C.; Lechuga, L. M.; Liz-Marzan, L. M. LSPR-based Nanobiosensors. *Nano Today* **2009**, *4*, 244-251.
- (32) Huang, X.; Liu, Y.; Yung, B.; Xiong, Y.; Chen, X. Nanotechnology-enhanced No-wash Biosensors for *In Vitro* Diagnostics of Cancer. *ACS Nano* **2017**, *11*, 5238-5292.
- (33) Howes, P. D.; Rana, S.; Stevens, M. M. Plasmonic Nanomaterials for Biodiagnostics. *Chem. Soc. Rev.* **2014**, *43*, 3835-3853.
- (34) Perfezou, M.; Turner, A.; Merkoci, A. Cancer Detection Using Nanoparticle-based Sensors. *Chem. Soc. Rev.* **2012**, *41*, 2606-2622.
- (35) Wu, X.; Xu, L.; Ma, W.; Liu, L.; Kuang, H.; Kotov, N. A.; Xu, C. Propeller-like Nanorod-upconversion Nanoparticle Assemblies with Intense Chiroptical Activity and Luminescence Enhancement in Aqueous Phase. *Adv. Mater.* **2016**, *28*, 5907-5915.
- (36) Rodriguez-Lorenzo, L.; de la Rica, R.; Alvarez-Puebla, R. A.; Liz-Marzan, L. M.; Stevens, M. M. Plasmonic Nanosensors with Inverse Sensitivity by Means of Enzyme-guided Crystal Growth. *Nat. Mater.* **2012**, *11*, 604-607.
- (37) Sun, X.; Guo, S.; Chung, C. S.; Zhu, W.; Sun, S. A Sensitive H₂O₂ Assay Based on Dumbbell-like PtPd-Fe₃O₄ Nanoparticles. *Adv. Mater.* **2013**, *25*, 132-136.
- (38) Zhu, H.; Sigdel, A.; Zhang, S.; Su, D.; Xi, Z.; Li, Q.; Sun, S. Core/Shell Au/MnO Nanoparticles Prepared Through Controlled Oxidation of AuMn as an Electrocatalyst for Sensitive H₂O₂ Detection. *Angew. Chem., Int. Ed.* **2014**, *53*, 12508-12512.
- (39) Hu, Y.; Cheng, H.; Zhao, X.; Wu, J.; Muhammad, F.; Lin, S.; He, J.; Zhou, L.; Zhang, C.; Deng, Y.; Wang, P.; Zhou, Z.; Nie, S.; Wei, H. Surface-enhanced Raman Scattering Active Gold Nanoparticles with Enzyme-mimicking Activities for Measuring Glucose and Lactate in Living Tissues. *ACS Nano* **2017**, *11*, 5558-5566.
- (40) Xie, J.; Zhang, Q.; Lee, J. Y.; Wang, D. I. The Synthesis of SERS-active Gold Nanoflower Tags for *In Vivo* Applications. *ACS Nano* **2008**, *2*, 2473-2480.

- (41) Gao, L.; Liu, M.; Ma, G.; Wang, Y.; Zhao, L.; Yuan, Q.; Gao, F.; Liu, R.; Zhai, J.; Chai, Z.; Zhao, Y.; Gao, X. Peptide-conjugated Gold Nanoprobe: Intrinsic Nanozyme-linked Immunsorbant Assay of Integrin Expression Level on Cell Membrane. *ACS Nano* **2015**, *9*, 10979-10990.
- (42) Liu, D.; Huang, X.; Wang, Z.; Jin, A.; Sun, X.; Zhu, L.; Wang, F.; Ma, Y.; Niu, G.; Hight Walker, A. R.; Chen, X. Gold Nanoparticle-based Activatable Probe for Sensing Ultralow Levels of Prostate-specific Antigen. *ACS Nano* **2013**, *7*, 5568-5576.
- (43) Ye, H.; Yang, K.; Tao, J.; Liu, Y.; Zhang, Q.; Habibi, S.; Nie, Z.; Xia, X. An Enzyme-free Signal Amplification Technique for Ultrasensitive Colorimetric Assay of Disease Biomarkers. *ACS Nano* **2017**, *11*, 2052-2059.
- (44) Bui, M. P.; Ahmed, S.; Abbas, A. Single-digit Pathogen and Attomolar Detection with the Naked Eye Using Liposome-amplified Plasmonic Immunoassay. *Nano Lett.* **2015**, *15*, 6239-6246.
- (45) Jana, N. R.; Gearheart, L.; Murphy, C. J. Seed-mediated Growth Approach for Shape-controlled Synthesis of Spheroidal and Rod-like Gold Nanoparticles Using a Surfactant Template. *Adv. Mater.* **2001**, *13*, 1389-1393.
- (46) Kang, Y.; Pyo, J. B.; Ye, X.; Diaz, R. E.; Gordon, T. R.; Stach, E. A.; Murray, C. B. Shape-controlled Synthesis of Pt Nanocrystals: the Role of Metal Carbonyls. *ACS Nano* **2013**, *7*, 645-653.
- (47) Xia, Y.; Xia, X.; Peng, H. C. Shape-controlled Synthesis of Colloidal Metal Nanocrystals: Thermodynamic versus Kinetic Products. *J. Am. Chem. Soc.* **2015**, 137, 7947-7966.
- (48) Tao, A. R.; Habas, S.; Yang, P. Shape Control of Colloidal Metal Nanocrystals. *Small* **2008**, 4, 310-325.
- (49) Xia, Y.; Xiong, Y.; Lim, B.; Skrabalak, S. E. Shape-controlled Synthesis of Metal Nanocrystals: Simple Chemistry Meets Complex Physics? *Angew. Chem.*, *Int. Ed.* **2009**, *48*, 60-103.
- (50) Hong, R.; Fischer, N. O.; Emrick, T.; Rotello, V. M. Surface PEGylation and Ligand Exchange Chemistry of FePt Nanoparticles for Biological Applications. *Chem. Mater.* **2005**, *17*, 4617-4621.
- (51) Latham, A. H.; Williams, M. E. Versatile Routes toward Functional, Water-soluble Nanoparticles via Trifluoroethylester-PEG-thiol Ligands. *Langmuir* **2006**, *22*, 4319-4326.
- (52) Palegrosdemange, C.; Simon, E. S.; Prime, K. L.; Whitesides, G. M. Formation of Self-assembled Monolayers by Chemisorption of Derivatives of Oligo(ethylene glycol) of Structure

- HS(CH₂)₁₁(OCH₂CH₂)_mOH on Gold. J. Am. Chem. Soc. **1991**, 113, 12-20.
- (53) Xia, X.; Yang, M.; Wang, Y.; Zheng, Y.; Li, Q.; Chen, J.; Xia, Y. Quantifying the Coverage Density of Poly(ethylene glycol) Chains on the Surface of Gold Nanostructures. *ACS Nano* **2012**, *6*, 512-522.
- (54) Yan, Y.; Wang, T.; Li, X.; Pang, H.; Xue, H. Noble Metal-based Materials in High-performance Supercapacitors. *Inorg. Chem. Front.* **2017**, *4*, 33-51.
- (55) Zhang, X.; Si, S.; Zhang, X.; Wu, W.; Xiao, X.; Jiang, C. Improved Thermal Stability of Graphene-veiled Noble Metal Nanoarrays as Recyclable SERS Substrates. *ACS Appl. Mater. Interfaces* **2017**, *9*, 40726-40733.
- (56) Xia, X.; Xia, Y. Gold Nanocages as Multifunctional Materials for Nanomedicine. *Front. Phys.* **2014**, 9, 378-384.
- (57) Kim, M. S.; Kweon, S. H.; Cho, S.; An, S. S. A.; Kim, M. I.; Doh, J.; Lee, J. Pt-decorated Magnetic Nanozymes for Facile and Sensitive Point-of-Care Bioassay. *ACS Appl. Mater. Interfaces* **2017**, *9*, 35133-35140.
- (58) Loynachan, C. N.; Thomas, M. R.; Gray, E. R.; Richards, D. A.; Kim, J.; Miller, B. S.; Brookes, J. C.; Agarwal, S.; Chudasama, V.; McKendry, R. A.; Stevens, M. M. Platinum Nanocatalyst Amplification: Redefining the Gold Standard for Lateral Flow Immunoassays with Ultrabroad Dynamic Range. *ACS Nano* **2018**, *12*, 279-288.
- (59) Zhu, Z.; Guan, Z.; Jia, S.; Lei, Z.; Lin, S.; Zhang, H.; Ma, Y.; Tian, Z.; Yang, C. Au@Pt Nanoparticle Encapsulated Target-responsive Hydrogel with Volumetric Bar-chart Chip Readout for Quantitative Point-of-Care Testing. *Angew. Chem., Int. Ed.* **2014**, *53*, 12503-12507.
- (60) Butler, S. A.; Khanlian, S. A.; Cole, L. A. Detection of Early Pregnancy Forms of Human Chorionic Gonadotropin by Home Pregnancy Test Devices. *Clin. Chem.* **2001**, *47*, 2131-2136.
- (61) Vanamerongen, A.; Wichers, J. H.; Berendsen, L. B. J. M.; Timmermans, A. J. M.; Keizer, G. D.; Vandoorn, A. W. J.; Bantjes, A.; Vangelder, W. M. J. Colloidal Carbon Particles as a New Label for Rapid Immunochemical Test Methods Quantitative Computer Image-analysis of Results. *J. Biotechnol.* **1993**, *30*, 185-195.
- (62) Leuvering, J. H.; Thal, P. J.; van der Waart, M.; Schuurs, A. H. Sol Particle Immunoassay (SPIA). *J. Immunoassay* **1980**, *1*, 77-91.
- (63) Kimling, J.; Maier, M.; Okenve, B.; Kotaidis, V.; Ballot, H.; Plech, A. Turkevich Method for Gold Nanoparticle Synthesis Revisited. *J. Phys. Chem. B* **2006**, *110*, 15700-15707.

- (64) Turkevich, J. Colloidal gold. Part II. Gold Bull. 1985, 18, 125-131.
- (65) Enustun, B. V.; Turkevich, J. Coagulation of Colloidal Gold. J. Am. Chem. Soc. 1963, 85, 3317-3328.
- (66) Nightingale, A. M.; Bannock, J. H.; Krishnadasan, S. H.; O'Mahony, F. T. F.; Haque, S. A.; Sloan, J.; Drury, C.; McIntyre, R.; deMello, J. C. Large-scale Synthesis of Nanocrystals in a Multichannel Droplet Reactor. *J. Mater. Chem. A* **2013**, *1*, 4067-4076.
- (67) Rathmell, A. R.; Bergin, S. M.; Hua, Y.; Li, Z.; Wiley, B. J. The Growth Mechanism of Copper Nanowires and Their Properties in Flexible, Transparent Conducting Films. *Adv. Mater.* **2010**, *22*, 3558-3563.
- (68) Wu, F.; Zhang, D.; Peng, M.; Yu, Z.; Wang, X.; Guo, G.; Sun, Y. Microfluidic Synthesis Enables Dense and Uniform Loading of Surfactant-free PtSn Nanocrystals on Carbon Supports for Enhanced Ethanol Oxidation. *Angew. Chem., Int. Ed.* **2016**, *55*, 4952-4956.
- (69) Lohse, S. E.; Eller, J. R.; Sivapalan, S. T.; Plews, M. R.; Murphy, C. J. A Simple Millifluidic Benchtop Reactor System for the High-throughput Synthesis and Functionalization of Gold Nanoparticles with Different Sizes and Shapes. *ACS Nano* **2013**, *7*, 4135-4150.
- (70) Liu, B.; Chen, H.; Liu, C.; Andrews, S. C.; Hahn, C.; Yang, P. Large-scale Synthesis of Transition-metal-doped TiO₂ Nanowires with Controllable Overpotential. *J. Am. Chem. Soc.* **2013**, *135*, 9995-9998.
- (71) Niu, G.; Zhang, L.; Ruditskiy, A.; Wang, L.; Xia, Y. A Droplet-reactor System Capable of Automation for the Continuous and Scalable Production of Noble-metal Nanocrystals. *Nano Lett.* **2018**, *18*, 3879-3884.
- (72) Lee, Y. W.; Kim, M.; Kang, S. W.; Han, S. W. Polyhedral Bimetallic Alloy Nanocrystals Exclusively Bound by {110} Facets: Au-Pd Rhombic Dodecahedra. *Angew. Chem., Int. Ed.* **2011**, 50, 3466-3470.
- (73) Sankar, M.; Dimitratos, N.; Miedziak, P. J.; Wells, P. P.; Kiely, C. J.; Hutchings, G. J. Designing Bimetallic Catalysts for a Green and Sustainable Future. *Chem. Soc. Rev.* **2012**, *41*, 8099-8139.
- (74) Chen, C.; Kang, Y.; Huo, Z.; Zhu, Z.; Huang, W.; Xin, H. L.; Snyder, J. D.; Li, D.; Herron, J. A.; Mavrikakis, M.; Chi, M.; More, K. L.; Li, Y.; Markovic, N. M.; Somorjai, G. A.; Yang, P.; Stamenkovic, V. R. Highly Crystalline Multimetallic Nanoframes with Three-dimensional Electrocatalytic Surfaces. *Science* **2014**, *343*, 1339-1343.

- (75) Hong, J. W.; Kang, S. W.; Choi, B. S.; Kim, D.; Lee, S. B.; Han, S. W. Controlled Synthesis of Pd-Pt Alloy Hollow Nanostructures with Enhanced Catalytic Activities for Oxygen Reduction. *ACS Nano* **2012**, *6*, 2410-2419.
- (76) Park, J.; Joo, J.; Kwon, S. G.; Jang, Y.; Hyeon, T. Synthesis of Monodisperse Spherical Nanocrystals. *Angew. Chem., Int. Ed.* **2007**, *46*, 4630-4660.
- (77) Rycenga, M.; Cobley, C. M.; Zeng, J.; Li, W.; Moran, C. H.; Zhang, Q.; Qin, D.; Xia, Y. Controlling the Synthesis and Assembly of Silver Nanostructures for Plasmonic Applications. *Chem. Rev.* **2011**, *111*, 3669-3712.
- (78) Murphy, C. J.; Sau, T. K.; Gole, A. M.; Orendorff, C. J.; Gao, J.; Gou, L.; Hunyadi, S. E.; Li, T. Anisotropic Metal Nanoparticles: Synthesis, Assembly, and Optical Applications. *J. Phys. Chem. B* **2005**, *109*, 13857-13870.
- (79) Daniel, M. C.; Astruc, D. Gold Nanoparticles: Assembly, Supramolecular Chemistry, Quantum-size-related Properties, and Applications toward Biology, Catalysis, and Nanotechnology. *Chem. Rev.* **2004**, *104*, 293-346.
- (80) Liu, X.; Atwater, M.; Wang, J.; Huo, Q. Extinction Coefficient of Gold Nanoparticles with Different Sizes and Different Capping Ligands. *Colloids Surf. B Biointerfaces* **2007**, *58*, 3-7.
- (81) Jain, P. K.; Lee, K. S.; El-Sayed, I. H.; El-Sayed, M. A. Calculated Absorption and Scattering Properties of Gold Nanoparticles of Different Size, Shape, and Composition: Applications in Biological Imaging and Biomedicine. *J. Phys. Chem. B* **2006**, *110*, 7238-7248.
- (82) Wiley, B. J.; Im, S. H.; Li, Z.; McLellan, J.; Siekkinen, A.; Xia, Y. Maneuvering the Surface Plasmon Resonance of Silver Nanostructures Through Shape-controlled Synthesis. *J. Phys. Chem. B* **2006**, *110*, 15666-15675.
- (83) Liang, H.; Wang, W.; Huang, Y.; Zhang, S.; Wei, H.; Xu, H. Controlled Synthesis of Uniform Silver Nanospheres. *J. Phys. Chem. C* **2010**, *114*, 7427-7431.
- (84) Bastus, N. G.; Merkoci, F.; Piella, J.; Puntes, V. Synthesis of Highly Monodisperse Citratestabilized Silver Nanoparticles of up to 200 nm: Kinetic Control and Catalytic Properties. *Chem. Mater.* **2014**, *26*, 2836-2846.
- (85) Luo, M.; Huang, H.; Choi, S. I.; Zhang, C.; da Silva, R. R.; Peng, H. C.; Li, Z.; Liu, J.; He, Z.; Xia, Y. Facile Synthesis of Ag Nanorods with No Plasmon Resonance Peak in the Visible Region by Using Pd Decahedra of 16 nm in Size as Seeds. *ACS Nano* **2015**, *9*, 10523-10532.
 - (86) Zhang, J.; Yang, H.; Fang, J.; Zou, S. Synthesis and Oxygen Reduction Activity of Shape-

- controlled Pt₃Ni Nanopolyhedra. Nano Lett. 2010, 10, 638-644.
- (87) Stamenkovic, V. R.; Fowler, B.; Mun, B. S.; Wang, G.; Ross, P. N.; Lucas, C. A.; Markovic, N. M. Improved Oxygen Reduction Activity on Pt₃Ni (111) via Increased Surface Site Availability. *Science* **2007**, *315*, 493-497.
- (88) Choi, S. I.; Herron, J. A.; Scaranto, J.; Huang, H.; Wang, Y.; Xia, X.; Lv, T.; Park, J. H.; Peng, H. C.; Mavrikakis, M.; Xia, Y. A Comprehensive Study of Formic Acid Oxidation on Palladium Nanocrystals with Different Types of Facets and Twin Defects. *Chemcatchem* **2015**, *7*, 2077-2084.
- (89) Lv, T.; Wang, Y.; Choi, S. I.; Chi, M. F.; Tao, J.; Pan, L.; Huang, C.; Zhu, Y.; Xia, Y. Controlled Synthesis of Nanosized Palladium Icosahedra and Their Catalytic Activity towards Formic Acid Oxidation. *Chemsuschem* **2013**, *6*, 1923-1930.
- (90) Thanh, N. T. K.; Green, L. A. W. Functionalisation of Nanoparticles for Biomedical Applications. *Nano Today* **2010**, *5*, 213-230.
- (91) Dreaden, E. C.; Alkilany, A. M.; Huang, X.; Murphy, C. J.; El-Sayed, M. A. The Golden Age: Gold Nanoparticles for Biomedicine. *Chem. Soc. Rev.* **2012**, *41*, 2740-2779.
- (92) Zhu, C.; Du, D.; Eychmuller, A.; Lin, Y. Engineering Ordered and Nonordered Porous Noble Metal Nanostructures: Synthesis, Assembly, and Their Applications in Electrochemistry. *Chem. Rev.* **2015**, *115*, 8896-8943.
- (93) Guo, S.; Zhang, S.; Sun, S. Tuning Nanoparticle Catalysis for the Oxygen Reduction Reaction. *Angew. Chem., Int. Ed.* **2013**, *52*, 8526-8544.
- (94) Sutter, E.; Jungjohann, K.; Bliznakov, S.; Courty, A.; Maisonhaute, E.; Tenney, S.; Sutter, P. *In situ* Liquid-cell Electron Microscopy of Silver-palladium Galvanic Replacement Reactions on Silver Nanoparticles. *Nat. Commun.* **2014**, *5*, 4946.
- (95) Yu, L.; Yan, Z.; Cai, Z.; Zhang, D.; Han, P.; Cheng, X.; Sun, Y. Quantitatively *in Situ* Imaging Silver Nanowire Hollowing Kinetics. *Nano Lett.* **2016**, *16*, 6555-6559.
- (96) Liao, H.; Zherebetskyy, D.; Xin, H.; Czarnik, C.; Ercius, P.; Elmlund, H.; Pan, M.; Wang, L. W.; Zheng, H. Facet Development During Platinum Nanocube Growth. *Science* **2014**, 345, 916-919.
- (97) Walsh, M. J.; Barrow, S. J.; Tong, W.; Funston, A. M.; Etheridge, J. Symmetry Breaking and Silver in Gold Nanorod Growth. *ACS Nano* **2015**, *9*, 715-724.
 - (98) Xie, S.; Choi, S. I.; Lu, N.; Roling, L. T.; Herron, J. A.; Zhang, L.; Park, J.; Wang, J.; Kim,

- M. J.; Xie, Z.; Mavrikakis, M.; Xia, Y. Atomic Layer-by-layer Deposition of Pt on Pd Nanocubes for Catalysts with Enhanced Activity and Durability toward Oxygen Reduction. *Nano Lett.* **2014**, *14*, 3570-3576.
- (99) LaMer, V. K.; Dinegar, R. H. Theory, Production and Mechanism of Formation of Monodispersed Hydrosols. *J. Am. Chem. Soc.* **1950**, *72*, 4847-4854.
- (100) Fan, F.; Liu, D.; Wu, Y.; Duan, S.; Xie, Z.; Jiang, Z.; Tian, Z. Epitaxial Growth of Heterogeneous Metal Nanocrystals: from Gold Nano-octahedra to Palladium and Silver Nanocubes. *J. Am. Chem. Soc.* **2008**, *130*, 6949-6951.
- (101) Xue, C.; Millstone, J. E.; Li, S.; Mirkin, C. A. Plasmon-driven Synthesis of Triangular Core-shell Nanoprisms from Gold Seeds. *Angew. Chem., Int. Ed.* **2007**, *46*, 8436-8439.
- (102) Habas, S. E.; Lee, H.; Radmilovic, V.; Somorjai, G. A.; Yang, P. Shaping Binary Metal Nanocrystals through Epitaxial Seeded Growth. *Nat. Mater.* **2007**, *6*, 692-697.
- (103) Sun, Y.; Gates, B.; Mayers, B.; Xia, Y. Crystalline Silver Nanowires by Soft Solution Processing. *Nano Lett.* **2002**, *2*, 165-168.
- (104) Jana, N. R.; Gearheart, L.; Murphy, C. J. Wet Chemical Synthesis of High Aspect Ratio Cylindrical Gold Nanorods. *J. Phys. Chem. B* **2001**, *105*, 4065-4067.
- (105) Xia, Y.; Xia, X.; Wang, Y.; Xie, S. Shape-controlled Synthesis of Metal Nanocrystals. *Mrs Bull.* **2013**, *38*, 335-344.
- (106) Xia, X.; Zeng, J.; Zhang, Q.; Moran, C. H.; Xia, Y. Recent Developments in Shape-controlled Synthesis of Silver Nanocrystals. *J Phys. Chem. C* **2012**, *116*, 21647-21656.
- (107) Xia, Y.; Gilroy, K. D.; Peng, H. C.; Xia, X. Seed-mediated Growth of Colloidal Metal Nanocrystals. *Angew. Chem., Int. Ed.* **2017**, *56*, 60-95.
- (108) Wade, L. G., Jr. Organic Chemistry, 2nd ed.; Prentice Hall: Englewood Cliffs, NJ, 1991.
- (109) Johnson, D. W.; Johnson, F. P. Joining Together: Group Theory and Group Skills, 4th ed. **1991**, Englewood Cliffs, NJ, US: Prentice-Hall, Inc.
- (110) Wang, Y.; He, J.; Liu, C.; Chong, W. H.; Chen, H. Thermodynamics versus Kinetics in Nanosynthesis. *Angew. Chem., Int. Ed.* **2015**, *54*, 2022-2051.
- (111) Zheng, Y.; Zhong, X.; Li, Z.; Xia, Y. Successive, Seed-mediated Growth for the Synthesis of Single-crystal Gold Nanospheres with Uniform Diameters Controlled in the Range of 5-150 nm. *Part. Part. Syst. Char.* **2014**, *31*, 266-273.
 - (112) Zhang, Q.; Li, W.; Moran, C.; Zeng, J.; Chen, J.; Wen, L. P.; Xia, Y. Seed-mediated

- Synthesis of Ag Nanocubes with Controllable Edge Lengths in the Range of 30-200 nm and Comparison of Their Optical Properties. *J. Am. Chem. Soc.* **2010**, *132*, 11372-11378.
- (113) Al-Saidi, W. A.; Feng, H. J.; Fichthorn, K. A. Adsorption of Polyvinylpyrrolidone on Ag Surfaces: Insight into a Structure-directing Agent. *Nano Lett.* **2012**, *12*, 997-1001.
- (114) Xia, X.; Zeng, J.; Oetjen, L. K.; Li, Q.; Xia, Y. Quantitative Analysis of the Role Played by Poly(vinylpyrrolidone) in Seed-mediated Growth of Ag Nanocrystals. *J. Am. Chem. Soc.* **2012**, *134*, 1793-801.
- (115) Homola, J. Surface Plasmon Resonance Sensors for Detection of Chemical and Biological Species. *Chem. Rev.* **2008**, *108*, 462-493.
- (116) Hoa, X. D.; Kirk, A. G.; Tabrizian, M. Towards Integrated and Sensitive Surface Plasmon Resonance Biosensors: A Review of Recent Progress. *Biosens Bioelectron.* **2007**, *23*, 151-160.
- (117) Eustis, S.; El-Sayed, M. A. Why Gold Nanoparticles Are More Precious Than Pretty Gold: Noble Metal Surface Plasmon Resonance and Its Enhancement of the Radiative and Nonradiative Properties of Nanocrystals of Different Shapes. *Chem. Soc. Rev.* **2006**, *35*, 209-217.
- (118) Teramura, Y.; Arima, Y.; Iwata, H. Surface Plasmon Resonance-based Highly Sensitive Immunosensing for Brain Natriuretic Peptide Using Nanobeads for Signal Amplification. *Anal. Biochem.* **2006**, *357*, 208-215.
- (119) Springer, T.; Homola, J. Biofunctionalized Gold Nanoparticles for SPR-biosensor-based Detection of CEA in Blood Plasma. *Anal. Bioanal. Chem.* **2012**, *404*, 2869-2875.
- (120) Huang, L.; Reekmans, G.; Saerens, D.; Friedt, J. M.; Frederix, F.; Francis, L.; Muyldermans, S.; Campitelli, A.; Van Hoof, C. Prostate-specific Antigen Immunosensing Based on Mixed Self-assembled Monolayers, Camel Antibodies and Colloidal Gold Enhanced Sandwich Assays. *Biosens Bioelectron.* **2005**, *21*, 483-490.
- (121) Liu, F.; Wong, M. M.; Chiu, S. K.; Lin, H.; Ho, J. C.; Pang, S. W. Effects of Nanoparticle Size and Cell Type on High Sensitivity Cell Detection Using a Localized Surface Plasmon Resonance Biosensor. *Biosens Bioelectron.* **2014**, *55*, 141-148.
- (122) He, L.; Smith, E. A.; Natan, M. J.; Keating, C. D. The Distance-dependence of Colloidal Au-amplified Surface Plasmon Resonance. *J. Phys. Chem. B* **2004**, *108*, 10973-10980.
- (123) Halpern, A. R.; Wood, J. B.; Wang, Y.; Corn, R. M. Single-nanoparticle Near-infrared Surface Plasmon Resonance Microscopy for Real-time Measurements of DNA Hybridization Adsorption. *ACS Nano* **2014**, *8*, 1022-1030.

- (124) Springer, T.; Ermini, M. L.; Spackova, B.; Jablonku, J.; Homola, J. Enhancing Sensitivity of Surface Plasmon Resonance Biosensors by Functionalized Gold Nanoparticles: Size Matters. *Anal. Chem.* **2014**, *86*, 10350-10356.
- (125) Yue, K.; Nan, J.; Zhang, X.; Tang, J.; Zhang, X., Photothermal Effects of Gold Nanoparticles Induced by Light Emitting Diodes. *Appl. Therm. Eng.* **2016**, *99*, 1093-1100.
- (126) Zeng, J.; Goldfeld, D.; Xia, Y. A Plasmon-assisted Optofluidic (PAOF) System for Measuring the Photothermal Conversion Efficiencies of Gold Nanostructures and Controlling an Electrical Switch. *Angew. Chem., Int. Ed.* **2013**, *52*, 4169-4173.
- (127) Zhan, L.; Guo, S.; Song, F.; Gong, Y.; Xu, F.; Boulware, D. R.; McAlpine, M. C.; Chan, W. C. W.; Bischof, J. C. The Role of Nanoparticle Design in Determining Analytical Performance of Lateral Flow Immunoassays. *Nano Lett.* **2017**, *17*, 7207-7212.
- (128) Ye, H.; Xia, X. Enhancing the Sensitivity of Colorimetric Lateral Flow Assay (CLFA) Through Signal Amplification Techniques. *J. Mater. Chem. B* **2018**, DOI:10.1039/C8TB01603H.
- (129) Hu, J.; Wang, S.; Wang, L.; Li, F.; Pingguan-Murphy, B.; Lu, T.; Xu, F. Advances in Paper-based Point-of-Care Diagnostics. *Biosens Bioelectron.* **2014**, *54*, 585-597.
- (130) Posthuma-Trumpie, G. A.; Korf, J.; van Amerongen, A. Lateral Flow (Immuno)Assay: Its Strengths, Weaknesses, Opportunities and Threats. A literature survey. *Anal. Bioanal. Chem.* **2009**, *393*, 569-582.
- (131) Bahadir, E. B.; Sezginturk, M. K. Lateral Flow Assays: Principles, Designs and Labels. *Trac-Trend. Anal. Chem.* **2016**, *82*, 286-306.
- (132) Lu, C. H.; Kalmar, B.; Malaspina, A.; Greensmith, L.; Petzold, A. A Method to Solubilise Protein Aggregates for Immunoassay Quantification which Overcomes the Neurofilament "Hook" Effect. *J. Neurosci. Methods* **2011**, *195*, 143-150.
- (133) Stamplecoskie, K. G.; Scaiano, J. C.; Tiwari, V. S.; Anis, H. Optimal Size of Silver Nanoparticles for Surface-enhanced Raman Spectroscopy. *J. Phys. Chem. C* **2011**, *115*, 1403-1409.
- (134) Vitos, L.; Ruban, A. V.; Skriver, H. L.; Kollar, J. The Surface Energy of Metals. *Surf. Sci.* **1998**, *411*, 186-202.
- (135) Yu, D.; Yam, V. W. Controlled Synthesis of Monodisperse Silver Nanocubes in Water. *J. Am. Chem. Soc.* **2004**, *126*, 13200-13201.
- (136) Jin, M.; Liu, H.; Zhang, H.; Xie, Z.; Liu, J.; Xia, Y. Synthesis of Pd Nanocrystals Enclosed by {100} Facets and with Sizes < 10 nm for Application in CO Oxidation. *Nano Res.* **2011**, *4*, 83-

91.

- (137) Gu, X.; Li, W. First-principles Study on the Origin of the Different Selectivities for Methanol Steam Reforming on Cu (111) and Pd (111). *J. Phys. Chem. C* **2010**, *114*, 21539-21547.
- (138) Huang, X.; Tang, S.; Mu, X.; Dai, Y.; Chen, G.; Zhou, Z.; Ruan, F.; Yang, Z.; Zheng, N. Freestanding Palladium Nanosheets with Plasmonic and Catalytic Properties. *Nat. Nanotechnol.* **2011**, *6*, 28-32.
- (139) Chen, G.; Tan, Y.; Wu, B.; Fu, G.; Zheng, N. Carbon Monoxide-controlled Synthesis of Surface-clean Pt Nanocubes with High Electrocatalytic Activity. *Chem. Commun.* **2012**, *48*, 2758-2760.
- (140) Palaikis, L.; Zurawski, D.; Hourani, M.; Wieckowski, A. Surface Electrochemistry of Carbon-monoxide Adsorbed from Electrolytic Solutions at Single-crystal Surfaces of Pt (111) and Pt (100). *Surf. Sci.* **1988**, *199*, 183-198.
- (141) Niu, Z.; Li, Y. Removal and Utilization of Capping Agents in Nanocatalysis. *Chem. Mater.* **2014**, *26*, 72-83.
- (142) Phan, C. M.; Nguyen, H. M. Role of Capping Agent in Wet Synthesis of Nanoparticles. *J. Phys. Chem. A* **2017**, *121*, 3213-3219.
- (143) Kilin, D. S.; Prezhdo, O. V.; Xia, Y. Shape-controlled Synthesis of Silver Nanoparticles: *Ab initio* Study of Preferential Surface Coordination with Citric Acid. *Chem. Phys. Lett.* **2008**, *458*, 113-116.
- (144) Xia, X.; Xie, S.; Liu, M.; Peng, H. C.; Lu, N.; Wang, J.; Kim, M. J.; Xia, Y. On the Role of Surface Diffusion in Determining the Shape or Morphology of Noble-metal Nanocrystals. *Proc. Natl. Acad. Sci. USA* **2013**, *110*, 6669-6673.
- (145) Xia, X.; Figueroa-Cosme, L.; Tao, J.; Peng, H. C.; Niu, G.; Zhu, Y.; Xia, Y. Facile Synthesis of Iridium Nanocrystals with Well-controlled Facets Using Seed-mediated Growth. *J. Am. Chem. Soc.* **2014**, *136*, 10878-10881.
- (146) Ye, H.; Wang, Q.; Catalano, M.; Lu, N.; Vermeylen, J.; Kim, M. J.; Liu, Y.; Sun, Y.; Xia, X. Ru Nanoframes with an *fcc* Structure and Enhanced Catalytic Properties. *Nano Lett.* **2016**, *16*, 2812-2817.
- (147) Xie, S.; Lu, N.; Xie, Z.; Wang, J.; Kim, M. J.; Xia, Y. Synthesis of Pd-Rh Core-frame Concave Nanocubes and Their Conversion to Rh Cubic Nanoframes by Selective Etching of the Pd Cores. *Angew. Chem., Int. Ed.* **2012**, *51*, 10266-10270.

- (148) Xia, X.; Choi, S. I.; Herron, J. A.; Lu, N.; Scaranto, J.; Peng, H. C.; Wang, J.; Mavrikakis, M.; Kim, M. J.; Xia, Y. Facile Synthesis of Palladium Right Bipyramids and Their Use as Seeds for Overgrowth and as Catalysts for Formic Acid Oxidation. *J. Am. Chem. Soc.* **2013**, *135*, 15706-15709.
- (149) Xia, X.; Xia, Y. Symmetry Breaking During Seeded Growth of Nanocrystals. *Nano Lett.* **2012**, *12*, 6038-6042.
- (150) Wang, Y.; Xie, S.; Liu, J.; Park, J.; Huang, C.; Xia, Y., Shape-controlled Synthesis of Palladium Nanocrystals: A Mechanistic Understanding of the Evolution from Octahedrons to Tetrahedrons. *Nano Lett.* **2013**, *13*, 2276-2281.
- (151) Jin, M.; Zhang, H.; Wang, J.; Zhong, X.; Lu, N.; Li, Z.; Xie, Z.; Kim, M. J.; Xia, Y. Copper Can Still be Epitaxially Deposited on Palladium Nanocrystals to Generate Core-shell Nanocubes Despite Their Large Lattice Mismatch. *ACS Nano* **2012**, *6*, 2566-2573.
- (152) Zeng, J.; Zhu, C.; Tao, J.; Jin, M.; Zhang, H.; Li, Z. Y.; Zhu, Y.; Xia, Y. Controlling the Nucleation and Growth of Silver on Palladium Nanocubes by Manipulating the Reaction Kinetics. *Angew. Chem., Int. Ed.* **2012**, *51*, 2354-2358.
- (153) Zhu, C.; Zeng, J.; Tao, J.; Johnson, M. C.; Schmidt-Krey, I.; Blubaugh, L.; Zhu, Y.; Gu, Z.; Xia, Y. Kinetically Controlled Overgrowth of Ag or Au on Pd Nanocrystal Seeds: from Hybrid Dimers to Nonconcentric and Concentric Bimetallic Nanocrystals. *J. Am. Chem. Soc.* **2012**, *134*, 15822-15831.
- (154) Kwon, M. J.; Lee, J.; Wark, A. W.; Lee, H. J. Nanoparticle-enhanced Surface Plasmon Resonance Detection of Proteins at Attomolar Concentrations: Comparing Different Nanoparticle Shapes and Sizes. *Anal. Chem.* **2012**, *84*, 1702-1707.
- (155) Zhang, H.; She, Z.; Su, H.; Kerman, K.; Kraatz, H. B. Effects of Bipyramidal Gold Nanoparticles and Gold Nanorods on the Detection of Immunoglobulins. *Analyst* **2016**, *141*, 6080-6086.
- (156) Peters, S. M.; Verheijen, M. A.; Prins, M. W.; Zijlstra, P. Strong Reduction of Spectral Heterogeneity in Gold Bipyramids for Single-particle and Single-molecule Plasmon Sensing. *Nanotechnology* **2016**, *27*, 024001.
- (157) Chen, H.; Kou, X.; Yang, Z.; Ni, W.; Wang, J. Shape- and Size-dependent Refractive Index Sensitivity of Gold Nanoparticles. *Langmuir* **2008**, *24*, 5233-5237.
 - (158) Graham, D.; Moskovits, M.; Tian, Z. Q. SERS Facts, Figures and the Future. Chem. Soc.

- Rev. 2017, 46, 3864-3865.
- (159) Kneipp, K.; Wang, Y.; Kneipp, H.; Perelman, L. T.; Itzkan, I.; Dasari, R. R.; Feld, M. S. Single Molecule Detection Using Surface-enhanced Raman Scattering (SERS). *Phys. Rev. Lett.* **1997**, *78*, 1667-1670.
- (160) Stiles, P. L.; Dieringer, J. A.; Shah, N. C.; Van Duyne, R. P. Surface-enhanced Raman Spectroscopy. *Annu. Rev. Anal. Chem.* **2008**, *1*, 601-626.
- (161) Banholzer, M. J.; Millstone, J. E.; Qin, L.; Mirkin, C. A. Rationally Designed Nanostructures for Surface-enhanced Raman Spectroscopy. *Chem. Soc. Rev.* **2008**, *37*, 885-897.
- (162) Dieringer, J. A.; Lettan, R. B.; Scheidt, K. A.; Van Duyne, R. P. A Frequency Domain Existence Proof of Single-molecule Surface-enhanced Raman Spectroscopy. *J. Am. Chem. Soc.* **2007**, *129*, 16249-16256.
- (163) Schlucker, S. Surface-enhanced Raman Spectroscopy: Concepts and Chemical Applications. *Angew. Chem., Int. Ed.* **2014**, *53*, 4756-4795.
- (164) Rycenga, M.; Xia, X.; Moran, C. H.; Zhou, F.; Qin, D.; Li, Z.; Xia, Y. Generation of Hot Spots with Silver Nanocubes for Single-molecule Detection by Surface-enhanced Raman Scattering. *Angew. Chem., Int. Ed.* **2011**, *50*, 5473-5477.
- (165) Senthil Kumar, P.; Pastoriza-Santos, I.; Rodriguez-Gonzalez, B.; Javier Garcia de Abajo, F.; Liz-Marzan, L. M. High-yield Synthesis and Optical Response of Gold Nanostars. *Nanotechnology* **2008**, *19*, 015606.
- (166) Mulvihill, M. J.; Ling, X.; Henzie, J.; Yang, P. Anisotropic Etching of Silver Nanoparticles for Plasmonic Structures Capable of Single-particle SERS. *J. Am. Chem. Soc.* **2010**, *132*, 268-274.
- (167) Xia, X.; Zeng, J.; McDearmon, B.; Zheng, Y.; Li, Q.; Xia, Y. Silver Nanocrystals with Concave Surfaces and Their Optical and Surface-enhanced Raman Scattering Properties. *Angew. Chem., Int. Ed.* **2011**, *50*, 12542-12546.
- (168) Hastings, S. P.; Swanglap, P.; Qian, Z.; Fang, Y.; Park, S. J.; Link, S.; Engheta, N.; Fakhraai, Z. Quadrupole-enhanced Raman Scattering. *ACS Nano* **2014**, *8*, 9025-9034.
- (169) Sanchez-Purra, M.; Carre-Camps, M.; de Puig, H.; Bosch, I.; Gehrke, L.; Hamad-Schifferli, K. Surface-enhanced Raman Spectroscopy-based Sandwich Immunoassays for Multiplexed Detection of Zika and Dengue Viral Biomarkers. *ACS Infect. Dis.* **2017**, *3*, 767-776.
- (170) Jv, Y.; Li, B.; Cao, R. Positively-charged Gold Nanoparticles as Peroxidase Mimic and Their Application in Hydrogen Peroxide and Glucose Detection. *Chem. Commun.* **2010**, *46*, 8017-

8019.

- (171) Wei, H.; Wang, E. Nanomaterials with Enzyme-like Characteristics (Nanozymes): Next Generation Artificial Enzymes. *Chem. Soc. Rev.* **2013**, *42*, 6060-6093.
- (172) He, W.; Wu, X.; Liu, J.; Hu, X.; Zhang, K.; Hou, S.; Zhou, W.; Xie, S. Design of AgM Bimetallic Alloy Nanostructures (M = Au, Pd, Pt) with Tunable Morphology and Peroxidase-like Activity. *Chem. Mater.* **2010**, *22*, 2988-2994.
- (173) He, W.; Liu, Y.; Yuan, J.; Yin, J.; Wu, X.; Hu, X.; Zhang, K.; Liu, J.; Chen, C.; Ji, Y.; Guo, Y. Au@Pt Nanostructures as Oxidase and Peroxidase Mimetics for Use in Immunoassays. *Biomaterials* **2011**, *32*, 1139-1147.
- (174) Ge, C.; Fang, G.; Shen, X.; Chong, Y.; Wamer, W. G.; Gao, X.; Chai, Z.; Chen, C.; Yin, J. Facet Energy versus Enzyme-like Activities: The Unexpected Protection of Palladium Nanocrystals against Oxidative Damage. *ACS Nano* **2016**, *10*, 10436-10445.
- (175) Liu, D.; Li, X.; Zhou, J.; Liu, S.; Tian, T.; Song, Y.; Zhu, Z.; Zhou, L.; Ji, T.; Yang, C. A Fully Integrated Distance Readout ELISA-chip for Point-of-Care Testing with Sample-in-answerout Capability. *Biosens Bioelectron.* **2017**, *96*, 332-338.
- (176) Liu, D.; Jia, S.; Zhang, H.; Ma, Y.; Guan, Z.; Li, J.; Zhu, Z.; Ji, T.; Yang, C. Integrating Target-responsive Hydrogel with Pressuremeter Readout Enables Simple, Sensitive, User-friendly, Quantitative Point-of-Care Testing. *ACS Appl. Mater. Interfaces* **2017**, *9*, 22252-22258.
- (177) Gao, Z.; Lv, S.; Xu, M.; Tang, D. High-index {hk0} Faceted Platinum Concave Nanocubes with Enhanced Peroxidase-like Activity for an Ultrasensitive Colorimetric Immunoassay of the Human Prostate-specific Antigen. *Analyst* **2017**, *142*, 911-917.
- (178) Watanabe, E.; Miyake, S.; Yogo, Y. Review of Enzyme-linked Immunosorbent Assays (ELISAs) for Analyses of Neonicotinoid Insecticides in Agro-environments. *J. Agric. Food Chem.* **2013**, *61*, 12459-12472.
- (179) Crowther, J. R. The ELISA Guidebook, 2nd Ed. **2009**, DOI: 10.1007/978-1-60327-254-4.
- (180) Lequin, R. M. Enzyme Immunoassay (EIA)/Enzyme-linked Immunosorbent Assay (ELISA). *Clin. Chem.* **2005**, *51*, 2415-2418.
- (181) Geddes, C. D.; Lakowicz, J. R. Editorial: Metal-Enhanced Fluorescence. *J. Fluorescence* **2002**, *12*, 121-129.
- (182) Aslan, K.; Lakowicz, J. R.; Geddes, C. D. Metal-enhanced Fluorescence Using Anisotropic Silver Nanostructures: Critical Progress to Date. *Anal. Bioanal. Chem.* **2005**, *382*, 926-933.

- (183) Yen, C. W.; de Puig, H.; Tam, J. O.; Gomez-Marquez, J.; Bosch, I.; Hamad-Schifferli, K.; Gehrke, L. Multicolored Silver Nanoparticles for Multiplexed Disease Diagnostics: Distinguishing Dengue, Yellow Fever, and Ebola Viruses. *Lab. Chip.* **2015**, *15*, 1638-1641.
- (184) Wang, Y.; Yang, X.; Bai, J.; Jiang, X.; Fan, G. High Sensitivity Hydrogen Peroxide and Hydrazine Sensor Based on Silver Nanocubes with Rich {100} Facets as an Enhanced Electrochemical Sensing Platform. *Biosens Bioelectron.* **2013**, *43*, 180-185.
- (185) Huang, Y.; Ferhan, A. R.; Dandapat, A.; Yoon, C. S.; Song, J. E.; Cho, E. C.; Kim, D. H. A Strategy for the Formation of Gold-Palladium Supra-nanoparticles from Gold Nanoparticles of Various Shapes and Their Application to High-performance H₂O₂ Sensing. *J. Phys. Chem. C* **2015**, *119*, 26164-26170.
- (186) Bauer, E.; van der Merwe, J. H. Structure and Growth of Crystalline Superlattices: From Monolayer to Superlattice. *Phys. Rev. B* **1986**, *33*, 3657-3671.
- (187) Zhang, L.; Roling, L. T.; Wang, X.; Vara, M.; Chi, M.; Liu, J.; Choi, S. I.; Park, J.; Herron, J. A.; Xie, Z.; Mavrikakis, M.; Xia, Y. Platinum-based Nanocages with Subnanometer-thick Walls and Well-defined, Controllable Facets. *Science* **2015**, *349*, 412-416.
- (188) Wang, X.; Choi, S. I.; Roling, L. T.; Luo, M.; Ma, C.; Zhang, L.; Chi, M.; Liu, J.; Xie, Z.; Herron, J. A.; Mavrikakis, M.; Xia, Y. Palladium-Platinum Core-shell Icosahedra with Substantially Enhanced Activity and Durability towards Oxygen Reduction. *Nat. Commun.* **2015**, *6*, 7594.
- (189) Weiner, R. G.; Kunz, M. R.; Skrabalak, S. E. Seeding a New Kind of Garden: Synthesis of Architecturally Defined Multimetallic Nanostructures by Seed-mediated Co-reduction. *Acc Chem Res* **2015**, *48*, 2688-2695.
- (190) Zhang, H.; Jin, M.; Wang, J.; Kim, M. J.; Yang, D.; Xia, Y. Nanocrystals Composed of Alternating Shells of Pd and Pt Can be Obtained by Sequentially Adding Different Precursors. *J. Am. Chem. Soc.* **2011**, *133*, 10422-10425.
- (191) Chen, M.; Wu, B.; Yang, J.; Zheng, N. Small Adsorbate-assisted Shape Control of Pd and Pt Nanocrystals. *Adv. Mater.* **2012**, *24*, 862-879.
- (192) Jakab, A.; Rosman, C.; Khalavka, Y.; Becker, J.; Trugler, A.; Hohenester, U.; Sonnichsen, C. Highly Sensitive Plasmonic Silver Nanorods. *ACS Nano* **2011**, *5*, 6880-6885.
- (193) Ye, H.; Liu, Y.; Chhabra, A.; Lilla, E.; Xia, X. Polyvinylpyrrolidone (PVP)-capped Pt Nanocubes with Superior Peroxidase-like Activity. *Chemnanomat* **2017**, *3*, 33-38.

- (194) Xia, X.; Zhang, J.; Lu, N.; Kim, M. J.; Ghale, K.; Xu, Y.; McKenzie, E.; Liu, J.; Ye, H. Pd-Ir Core-shell Nanocubes: A Type of Highly Efficient and Versatile Peroxidase Mimic. *ACS Nano* **2015**, *9*, 9994-10004.
- (195) Liu, A.; Geng, H.; Xu, C.; Qiu, H. A Three-dimensional Hierarchical Nanoporous PdCu Alloy for Enhanced Electrocatalysis and Biosensing. *Anal. Chim. Acta.* **2011**, *703*, 172-178.
- (196) Xu, C.; Liu, Y.; Su, F.; Liu, A.; Qiu, H. Nanoporous PtAg and PtCu Alloys with Hollow Ligaments for Enhanced Electrocatalysis and Glucose Biosensing. *Biosens Bioelectron.* **2011**, *27*, 160-166.
- (197) Gao, Z.; Ye, H.; Tang, D.; Tao, J.; Habibi, S.; Minerick, A.; Tang, D.; Xia, X. Platinum-decorated Gold Nanoparticles with Dual Functionalities for Ultrasensitive Colorimetric *in Vitro* Diagnostics. *Nano Lett.* **2017**, *17*, 5572-5579.
- (198) Josephy, P. D.; Eling, T.; Mason, R. P. The Horseradish Peroxidase-catalyzed Oxidation of 3,5,3',5'-Tetramethylbenzidine: Free Radical and Charge-transfer Complex Intermediates. *J Biol. Chem.* **1982**, *257*, 3669-3675.
- (199) Wu, J.; Qin, K.; Yuan, D.; Tan, J.; Qin, L.; Zhang, X.; Wei, H. Rational Design of Au@Pt Multibranched Nanostructures as Bifunctional Nanozymes. *ACS Appl. Mater. Interfaces* **2018**, *10*, 12954-12959.
- (200) Link, S.; El-Sayed, M. A. Spectral Properties and Relaxation Dynamics of Surface Plasmon Electronic Oscillations in Gold and Silver Nanodots and Nanorods. *J. Phys. Chem. B* **1999**, *103*, 8410-8426.
- (201) Mulvaney, P. Surface Plasmon Spectroscopy of Nanosized Metal Particles. *Langmuir* **1996**, *12*, 788-800.
- (202) Lopez-Lozano, X.; Mottet, C.; Weissker, H. C. Effect of Alloying on the Optical Properties of Ag-Au Nanoparticles. *J. Phys. Chem. C* **2013**, *117*, 3062-3068.
- (203) Xiu, Z.; Ma, J.; Alvarez, P. J. Differential Effect of Common Ligands and Molecular Oxygen on Antimicrobial Activity of Silver Nanoparticles versus Silver Ions. *Environ. Sci. Technol.* **2011**, *45*, 9003-9008.
- (204) Liu, J.; Sonshine, D. A.; Shervani, S.; Hurt, R. H. Controlled Release of Biologically Active Silver from Nanosilver Surfaces. *ACS Nano* **2010**, *4*, 6903-6913.
- (205) Levard, C.; Hotze, E. M.; Lowry, G. V.; Brown, G. E. Jr. Environmental Transformations of Silver Nanoparticles: Impact on Stability and Toxicity. *Environ. Sci. Technol.* **2012**, *46*, 6900-

- 6914.
- (206) Yang, Y.; Liu, J.; Fu, Z. W.; Qin, D. Galvanic Replacement-free Deposition of Au on Ag for Core-shell Nanocubes with Enhanced Chemical Stability and SERS Activity. *J. Am. Chem. Soc.* **2014**, *136*, 8153-8156.
- (207) Gao, C.; Hu, Y.; Wang, M.; Chi, M.; Yin, Y. Fully Alloyed Ag/Au Nanospheres: Combining the Plasmonic Property of Ag with the Stability of Au. *J. Am. Chem. Soc.* **2014**, *136*, 7474-7479.
- (208) Casillas, G.; Velazquez-Salazar, J. J.; Jose-Yacaman, M. A New Mechanism of Stabilization of Large Decahedral Nanoparticles. *J. Phys. Chem. C* **2012**, *116*, 8844-8848.
- (209) Wang, Y.; Peng, H. C.; Liu, J.; Huang, C.; Xia, Y. Use of Reduction Rate as a Quantitative Knob for Controlling the Twin Structure and Shape of Palladium Nanocrystals. *Nano Lett.* **2015**, *15*, 1445-1450.
- (210) Im, S. H.; Lee, Y. T.; Wiley, B.; Xia, Y. Large-scale Synthesis of Silver Nanocubes: the Role of HCl in Promoting Cube Perfection and Monodispersity. *Angew. Chem., Int. Ed.* **2005**, *44*, 2154-2157.
- (211) Wiley, B.; Herricks, T.; Sun, Y.; Xia, Y. Polyol Synthesis of Silver Nanoparticles: Use of Chloride and Oxygen to Promote the Formation of Single-crystal, Truncated Cubes and Tetrahedrons. *Nano Lett.* **2004**, *4*, 1733-1739.
- (212) Long, R.; Zhou, S.; Wiley, B. J.; Xiong, Y. Oxidative Etching for Controlled Synthesis of Metal Nanocrystals: Atomic Addition and Subtraction. *Chem. Soc. Rev.* **2014**, *43*, 6288-6310.
- (213) Duan, H.; Yan, N.; Yu, R.; Chang, C. R.; Zhou, G.; Hu, H.; Rong, H.; Niu, Z.; Mao, J.; Asakura, H.; Tanaka, T.; Dyson, P. J.; Li, J.; Li, Y. Ultrathin Rhodium Nanosheets. *Nat. Commun.* **2014**, *5*, 3093.
- (214) Huang, X.; Li, S.; Huang, Y.; Wu, S.; Zhou, X.; Li, S.; Gan, C.; Boey, F.; Mirkin, C. A.; Zhang, H. Synthesis of Hexagonal Close-packed Gold nanostructures. *Nat. Commun.* **2011**, *2*, 292.
- (215) Chakraborty, I.; Carvalho, D.; Shirodkar, S. N.; Lahiri, S.; Bhattacharyya, S.; Banerjee, R.; Waghmare, U.; Ayyub, P. Novel Hexagonal Polytypes of Silver: Growth, Characterization and First-principles Calculations. *J. Phys. Condens. Matter.* **2011**, *23*, 325401.
- (216) Liu, X.; Luo, J.; Zhu, J. Size Effect on the Crystal Structure of Silver Nanowires. *Nano Lett.* **2006**, *6*, 408-412.
- (217) Guo, Q.; Zhao, Y.; Mao, W. L.; Wang, Z.; Xiong, Y.; Xia, Y. Cubic to Tetragonal Phase Transformation in Cold-compressed Pd Nanocubes. *Nano Lett.* **2008**, *8*, 972-975.

- (218) Fan, Z.; Zhang, H. Crystal Phase-controlled Synthesis, Properties and Applications of Noble Metal Nanomaterials. *Chem. Soc. Rev.* **2016**, *45*, 63-82.
- (219) Wang, X.; Feng, J.; Bai, Y.; Zhang, Q.; Yin, Y. Synthesis, Properties, and Applications of Hollow Micro-/Nanostructures. *Chem. Rev.* **2016**, *116*, 10983-1060.
- (220) Ataee-Esfahani, H.; Nemoto, Y.; Wang, L.; Yamauchi, Y. Rational Synthesis of Pt Spheres with Hollow Interior and Nanosponge Shell Using Silica Particles as Template. *Chem. Commun.* **2011**, *47*, 3885-3887.
- (221) Kim, S. W.; Kim, M.; Lee, W. Y.; Hyeon, T. Fabrication of Hollow Palladium Spheres and Their Successful Application to the Recyclable Heterogeneous Catalyst for Suzuki Coupling Reactions. *J. Am. Chem. Soc.* **2002**, *124*, 7642-7643.
- (222) Chen, G.; Desinan, S.; Rosei, R.; Rosei, F.; Ma, D. Hollow Ruthenium Nanoparticles with Small Dimensions Derived from Ni@Ru Core@Shell Structure: Synthesis and Enhanced Catalytic Dehydrogenation of Ammonia Borane. *Chem. Commun.* **2012**, *48*, 8009-8011.
- (223) He, D.; He, D.; Wang, J.; Lin, Y.; Yin, P.; Hong, X.; Wu, Y.; Li, Y. Ultrathin Icosahedral Ptenriched Nanocage with Excellent Oxygen Reduction Reaction Activity. *J. Am. Chem. Soc.* **2016**, *138*, 1494-1497.
- (224) Yu, L.; Zhang, L.; Wu, H.; Lou, X. Formation of Ni_xCo_{3-x}S₄ Hollow Nanoprisms with Enhanced Pseudocapacitive Properties. *Angew. Chem., Int. Ed.* **2014**, *53*, 3711-3714.
- (225) Ostwald, W. Studien über die Bildung und Umwandlung fester Körper. Z. Phys. Chem. **1897**, 22, 289-330.
- (226) Liang, H.; Zhang, H.; Hu, J.; Guo, Y.; Wan, L.; Bai, C. Pt Hollow Nanospheres: Facile Synthesis and Enhanced Electrocatalysts. *Angew. Chem., Int. Ed.* **2004**, *43*, 1540-1543.
- (227) Sun, Y.; Mayers, B. T.; Xia, Y. Template-engaged Replacement Reaction: A One-step Approach to the Large-scale Synthesis of Metal Nanostructures with Hollow Interiors. *Nano Lett.* **2002**, *2*, 481-485.
- (228) Zhou, W.; Chen, W.; Nai, J.; Yin, P.; Chen, C.; Guo, L. Selective Synthesis of Peapodlike Ni/Ni₃S₂ Nanochains and Nickel Sulfide Hollow Chains and Their Magnetic Properties. *Adv. Funct. Mater.* **2010**, *20*, 3678-3683.
- (229) Yin, Y.; Rioux, R. M.; Erdonmez, C. K.; Hughes, S.; Somorjai, G. A.; Alivisatos, A. P. Formation of Hollow Nanocrystals Through the Nanoscale Kirkendall Effect. *Science* **2004**, *304*, 711-714.

- (230) Skrabalak, S. E.; Chen, J.; Sun, Y.; Lu, X.; Au, L.; Cobley, C. M.; Xia, Y. Gold Nanocages: Synthesis, Properties, and Applications. *Acc. Chem. Res.* **2008**, 41, 1587-1595.
- (231) Xia, X.; Wang, Y.; Ruditskiy, A.; Xia, Y. 25th Anniversary Article: Galvanic Replacement: A Simple and Versatile Route to Hollow Nanostructures with Tunable and Well-controlled Properties. *Adv. Mater.* **2013**, *25*, 6313-6333.
- (232) Hong, X.; Wang, D.; Cai, S.; Rong, H.; Li, Y. Single-crystalline Octahedral Au-Ag Nanoframes. *J. Am. Chem. Soc.* **2012**, *134*, 18165-18168.
- (233) Wang, Z. L.; Ahmad, T. S.; El-Sayed, M. A. Steps, Ledges and Kinks on the Surfaces of Platinum Nanoparticles of Different Shapes. *Surf. Sci.* **1997**, *380*, 302-310.
- (234) Gonzalez, E.; Arbiol, J.; Puntes, V. F. Carving at the Nanoscale: Sequential Galvanic Exchange and Kirkendall Growth at Room Temperature. *Science* **2011**, *334*, 1377-1380.
- (235) Sun, X.; Kim, J.; Gilroy, K. D.; Liu, J.; König, T. A. F.; Qin, D. Gold-based Cubic Nanoboxes with Well-defined Openings at the Corners and Ultrathin Walls Less Than Two Nanometers Thick. *ACS Nano* **2016**, *10*, 8019-8025.
- (236) Prodan, E.; Radloff, C.; Halas, N. J.; Nordlander, P. A Hybridization Model for the Plasmon Response of Complex Nanostructures. *Science* **2003**, *302*, 419-422.
- (237) Mahmoud, M. A.; El-Sayed, M. A. Gold Nanoframes: Very High Surface Plasmon Fields and Excellent Near-infrared Sensors. *J. Am. Chem. Soc.* **2010**, *132*, 12704-12710.
- (238) Mahmoud, M. A.; O'Neil, D.; El-Sayed, M. A. Hollow and Solid Metallic Nanoparticles in Sensing and in Nanocatalysis. *Chem. Mater.* **2014**, *26*, 44-58.
- (239) Mahmoud, M. A.; Snyder, B.; El-Sayed, M. A. Surface Plasmon Fields and Coupling in the Hollow Gold Nanoparticles and Surface-enhanced Raman Spectroscopy. Theory and Experiment. *J. Phys. Chem. C* **2010**, *114*, 7436-7443.
- (240) Genc, A.; Patarroyo, J.; Sancho-Parramon, J.; Arenal, R.; Duchamp, M.; Gonzalez, E. E.; Henrard, L.; Bastus, N. G.; Dunin-Borkowski, R. E.; Puntes, V. F.; Arbiol, J. Tuning the Plasmonic Response up: Hollow Cuboid Metal Nanostructures. *ACS Photonics* **2016**, *3*, 770-779.
- (241) Hohenester, U. Simulating Electron Energy Loss Spectroscopy with the MNPBEM Toolbox. *Comput. Phys. Commun.* **2014**, *185*, 1177-1187.
- (242) Lim, D. K.; Jeon, K. S.; Hwang, J. H.; Kim, H.; Kwon, S.; Suh, Y. D.; Nam, J. M. Highly Uniform and Reproducible Surface-enhanced Raman Scattering from DNA-tailorable Nanoparticles with 1-nm Interior Gap. *Nat. Nanotechnol.* **2011**, *6*, 452-460.

- (243) Zhang, W.; Rahmani, M.; Niu, W.; Ravaine, S.; Hong, M.; Lu, X. Tuning Interior Nanogaps of Double-shelled Au/Ag Nanoboxes for Surface-enhanced Raman Scattering. *Sci. Rep.* **2015**, *5*, 8382.
- (244) Camposeo, A.; Persano, L.; Manco, R.; Wang, Y.; Del Carro, P.; Zhang, C.; Li, Z.; Pisignano, D.; Xia, Y. Metal-enhanced Near-infrared Fluorescence by Micropatterned Gold Nanocages. *ACS Nano* **2015**, *9*, 10047-10054.
- (245) Park, J. E.; Kim, S.; Son, J.; Lee, Y.; Nam, J. M. Highly Controlled Synthesis and Super-Radiant Photoluminescence of Plasmonic Cube-in-cube Nanoparticles. *Nano Lett.* **2016**, *16*, 7962-7967.
- (246) Cho, E. C.; Zhang, Q.; Xia, Y. The Effect of Sedimentation and Diffusion on Cellular Uptake of Gold Nanoparticles. *Nat. Nanotechnol.* **2011**, *6*, 385-391.
- (247) Lim, D. K.; Jeon, K. S.; Kim, H. M.; Nam, J. M.; Suh, Y. D. Nanogap-engineerable Ramanactive Nanodumbbells for Single-molecule Detection. *Nat. Mater.* **2010**, *9*, 60-67.
- (248) Xu, L.; Yan, W.; Ma, W.; Kuang, H.; Wu, X.; Liu, L.; Zhao, Y.; Wang, L.; Xu, C. SERS Encoded Silver Pyramids for Attomolar Detection of Multiplexed Disease Biomarkers. *Adv. Mater.* **2015**, *27*, 1706-1711.
- (249) Wu, X.; Xu, L.; Liu, L.; Ma, W.; Yin, H.; Kuang, H.; Wang, L.; Xu, C.; Kotov, N. A. Unexpected Chirality of Nanoparticle Dimers and Ultrasensitive Chiroplasmonic Bioanalysis. *J. Am. Chem. Soc.* **2013**, *135*, 18629-18636.
- (250) Kang, T.; Yoo, S. M.; Yoon, I.; Lee, S. Y.; Kim, B. Patterned Multiplex Pathogen DNA Detection by Au Particle-on-wire SERS Sensor. *Nano Lett.* **2010**, 10, 1189-1193.
- (251) de la Rica, R.; Stevens, M. M. Plasmonic ELISA for the Ultrasensitive Detection of Disease Biomarkers with the Naked Eye. *Nat. Nanotechnol.* **2012**, 7, 821-824.
- (252) Xu, S.; Ouyang, W.; Xie, P.; Lin, Y.; Qiu, B.; Lin, Z.; Chen, G.; Guo, L. Highly Uniform Gold Nanobipyramids for Ultrasensitive Colorimetric Detection of Influenza Virus. *Anal. Chem.* **2017**, *89*, 1617-1623.
- (253) Liu, D.; Yang, J.; Wang, H.; Wang, Z.; Huang, X.; Wang, Z.; Niu, G.; Hight Walker, A. R.; Chen, X. Glucose Oxidase-catalyzed Growth of Gold Nanoparticles Enables Quantitative Detection of Attomolar Cancer Biomarkers. *Anal. Chem.* **2014**, *86*, 5800-5806.
- (254) Yang, X.; Yu, Y.; Gao, Z. A Highly Sensitive Plasmonic DNA Assay Based on Triangular Silver Nanoprism Etching. *ACS Nano* **2014**, *8*, 4902-4907.

- (255) Sun, Z.; Zhao, Q.; Zhang, G.; Li, Y.; Zhang, G.; Zhang, F.; Fan, X. Exfoliated MoS₂ Supported Au-Pd Bimetallic Nanoparticles with Core-shell Structures and Superior Peroxidase-like Activities. *RSC Adv.* **2015**, *5*, 10352-10357.
- (256) Xiao, L.; Zhu, A.; Xu, Q.; Chen, Y.; Xu, J.; Weng, J. Colorimetric Biosensor for Detection of Cancer Biomarker by Au Nanoparticle-decorated Bi₂Se₃ Nanosheets. *ACS Appl. Mater. Interfaces* **2017**, *9*, 6931-6940.
- (257) Liu, M.; Zhao, H.; Chen, S.; Yu, H.; Quan, X. Interface Engineering Catalytic Graphene for Smart Colorimetric Biosensing. *ACS Nano* **2012**, *6*, 3142-3151.
- (258) Tao, Y.; Lin, Y.; Huang, Z.; Ren, J.; Qu, X. Incorporating Graphene Oxide and Gold Nanoclusters: A Synergistic Catalyst with Surprisingly High Peroxidase-like Activity over a Broad pH Range and Its Application for Cancer Cell Detection. *Adv. Mater.* **2013**, *25*, 2594-2599.
- (259) Cai, S.; Liu, X.; Han, Q.; Qi, C.; Yang, R.; Wang, C. A Novel Strategy to Construct Supported Pd Nanocomposites with Synergistically Enhanced Catalytic Performances. *Nano Res.* **2018**, *11*, 3272-3281.
- (260) Jazayeri, M. H.; Amani, H.; Pourfatollah, A. A.; Pazoki-Toroudi, H.; Sedighimoghaddam, B. Various Methods of Gold Nanoparticles (GNPs) Conjugation to Antibodies. *Sens. Biosensing Res.* **2016**, *9*, 17-22.
- (261) Jana, D.; Matti, C.; He, J.; Sagle, L. Capping Agent-free Gold Nanostars Show Greatly Increased Versatility and Sensitivity for Biosensing. *Anal. Chem.* **2015**, *87*, 3964-3972.
- (262) Li, D.; Wang, C.; Tripkovic, D.; Sun, S.; Markovic, N. M.; Stamenkovic, V. R. Surfactant Removal for Colloidal Nanoparticles from Solution Synthesis: The Effect on Catalytic Performance. *ACS Catal.* **2012**, *2*, 1358-1362.
- (263) Liu, Y.; Wang, C.; Wei, Y.; Zhu, L.; Li, D.; Jiang, J.; Markovic, N. M.; Stamenkovic, V. R.; Sun, S. Surfactant-induced Postsynthetic Modulation of Pd Nanoparticle Crystallinity. *Nano Lett.* **2011**, *11*, 1614-1617.
- (264) Liu, Y.; Liu, Y.; Yin, J.; Nie, Z. Self-assembly of Amphiphilic Block Copolymer-tethered Nanoparticles: A New Approach to Nanoscale Design of Functional Materials. *Macromol. Rapid Commun.* **2015**, *36*, 711-725.
- (265) He, J.; Liu, Y.; Babu, T.; Wei, Z.; Nie, Z. Self-assembly of Inorganic Nanoparticle Vesicles and Tubules Driven by Tethered Linear Block Copolymers. *J. Am. Chem. Soc.* **2012**, *134*, 11342-11345.

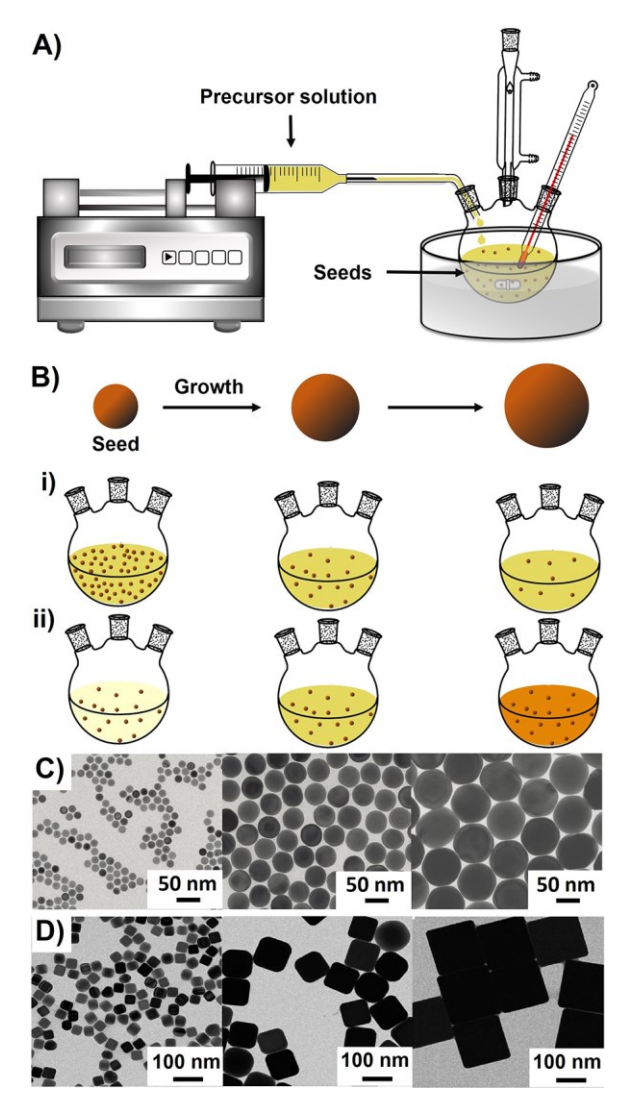


Figure 1. (A) Schematics showing a typical setup for seeded growth of colloidal noble-metal nanostructures. (B) Schematics showing size control in a seeded growth that can be achieved by altering: *i*) the number of seeds, or *ii*) the concentration of metal precursor. (C) Transmission electron microscope (TEM) images of Au nanospheres with average diameters of 15, 46 and 80 nm (from left to right). Adapted with permission from ref 111. Copyright 2013 Wiley-VCH. (D) TEM images of Ag nanocubes with average edge lengths of 36, 99 and 172 nm (from left to right). Adapted with permission from ref 112. Copyright 2010 American Chemical Society.

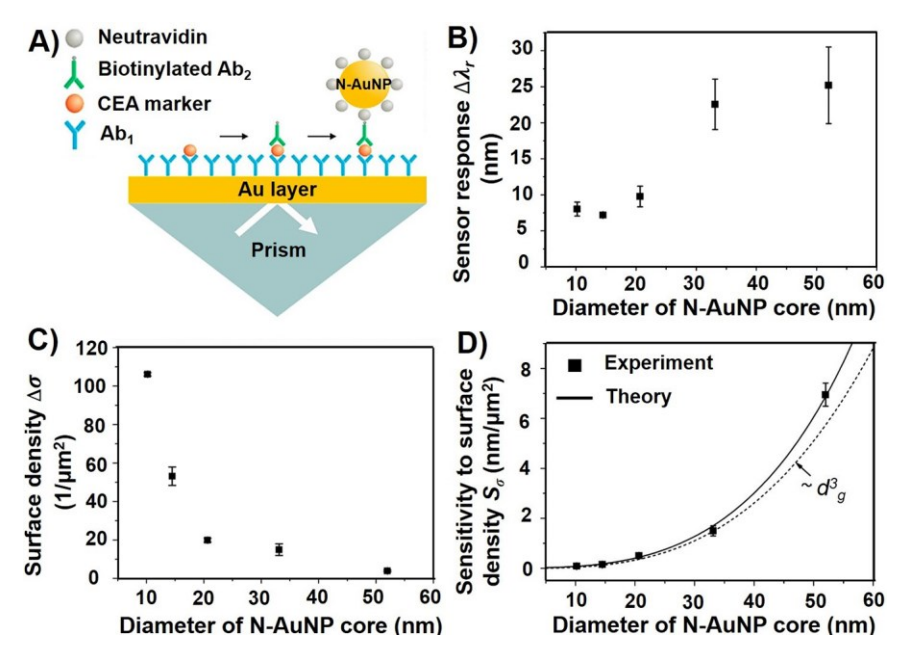


Figure 2. (A) Schematics showing the sandwich assay of carcinoembryonic antigen (CEA) by a neutravidin-functionalized AuNPs (N-AuNPs)-enhanced SPR sensor. N-AuNPs with Au cores of five different sizes (*i.e.*, diameters of 10, 15, 21, 33, and 52 nm) are evaluated in the sensor. (B) Sensor responses ($\Delta \lambda_r$) for N-AuNPs with different sizes. (C) Surface densities ($\Delta \sigma$) for N-AuNPs with different sizes. (D) Theoretical and experimental sensor sensitivity to surface density (S_σ) as a function of N-AuNP size. The dotted line represents a cubic dependence of S_σ on the AuNP size. Adapted with permission from ref 124. Copyright 2014 American Chemical Society.

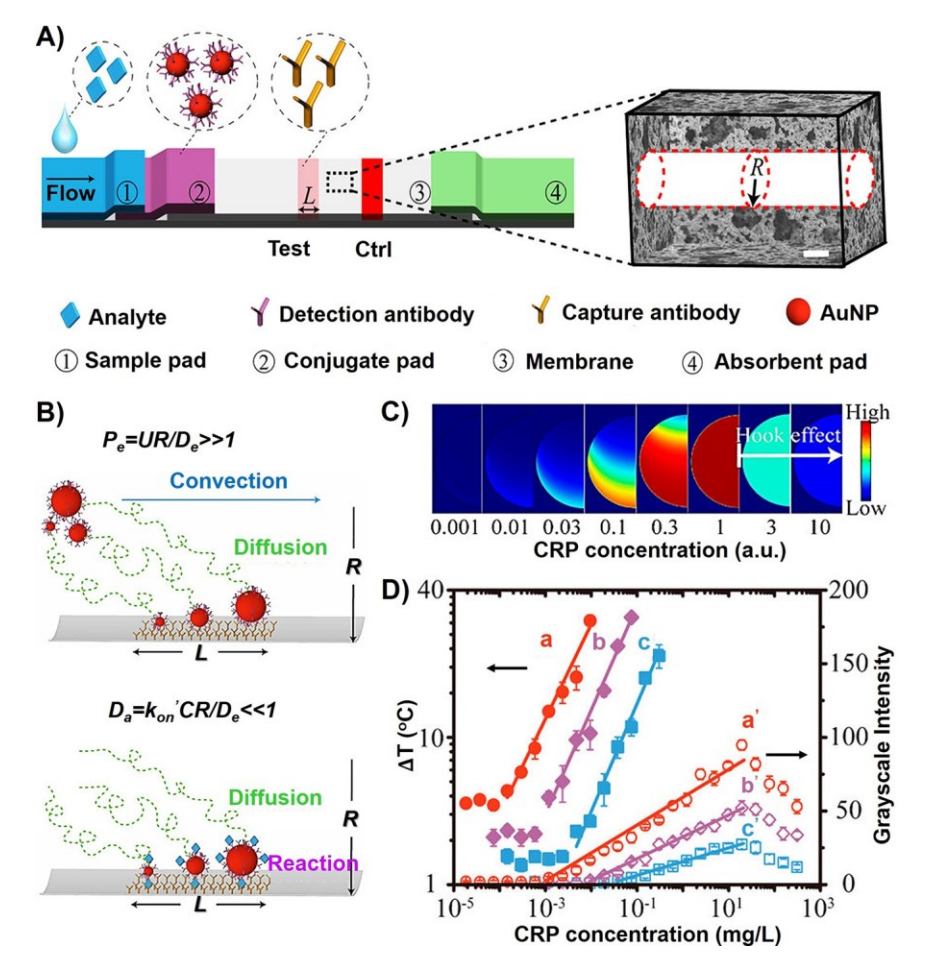


Figure 3. (A) Schematics showing the architecture of a typical AuNP-based LFA with test line width *L*, where the nitrocellulose membrane is conceptually simplified as bundles of cylindrical pores with radius *R*. Ctrl represents the control line of LFA. AuNPs of 30, 60, and 100 nm in diameters are studied in the LFA. (B) Peclet number (P_e) and Damkohler number (D_a) that were used to assess the factors of convection, diffusion, and reaction in LFA. Reaction is recognized to be the rate-limiting step of AuNP capture in the test zone. (C) COMSOL modeling result showing the capture of 100 nm AuNP in the test zone of sandwich LFA of C-reactive protein (CRP). (D) Experimental thermal (solid symbols) and visual (hollow symbols) signals of CRP LFAs. a/a', b/b', and c/c' denote the results for 100 nm, 60 nm, 30 nm AuNPs, respectively. Adapted with permission from ref 127. Copyright 2017 American Chemical Society.

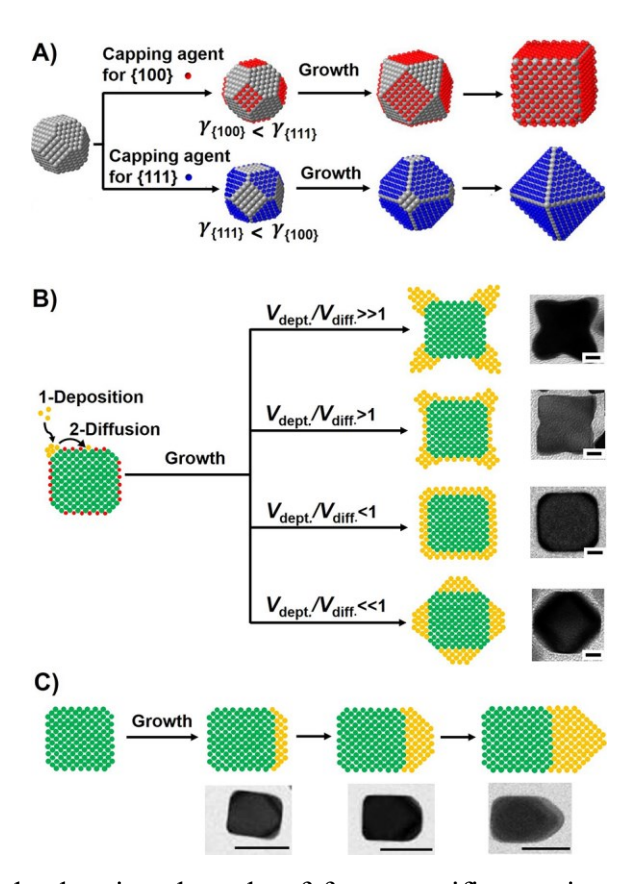


Figure 4. (A) 3D models showing the role of facet-specific capping agents in controlling the growth pathway of a cuboctahedral seed with an *fcc* crystal structure. Adapted with permission from ref 47. Copyright 2015 American Chemical Society. (B) 2D models and TEM images (scale bars: 50 nm) showing the shape evolution of a cubic seed under four different kinetic conditions. The side faces of the cubic seed are covered by capping agents (red dots). Adapted with permission from ref 144. Copyright 2013 National Academy of Sciences. (C) 2D models and TEM images (scale bars: 50 nm) showing the selective growth along one of the six side faces of a cubic seed. Adapted with permission from ref 149. Copyright 2012 American Chemical Society.

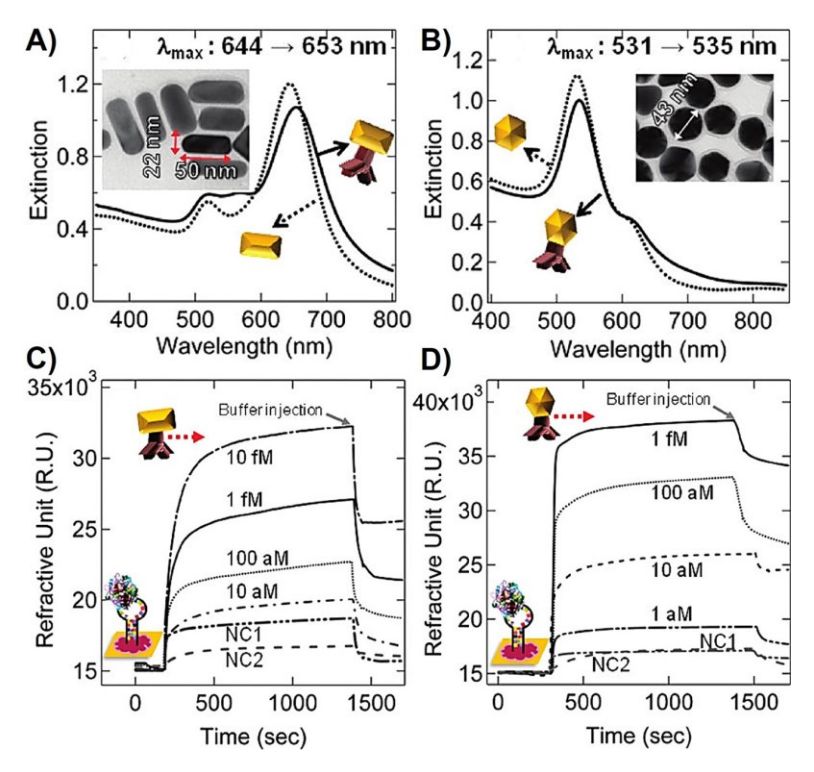


Figure 5. (A, B) UV-vis spectra taken from aqueous suspensions of Au nanorods (A) and Au quasi-spherical nanoparticles (B) before (dashed lines) and after (solid lines) they had been conjugated with anti-thrombin antibodies. Insets show TEM images of corresponding Au nanostructures. (C, D) SPR sensorgrams for the detection of thrombin using Au nanorods (C) and Au quasi-spherical nanoparticles (D) as the signal enhancers. NC1 and NC2 represent nonspecific signal recorded from anti-thrombin conjugated Au nanostructures in the absence of thrombin and anti-BSA conjugated Au nanostructures in the presence of thrombin, respectively. Reprinted with permission from ref 154. Copyright 2012 American Chemical Society.

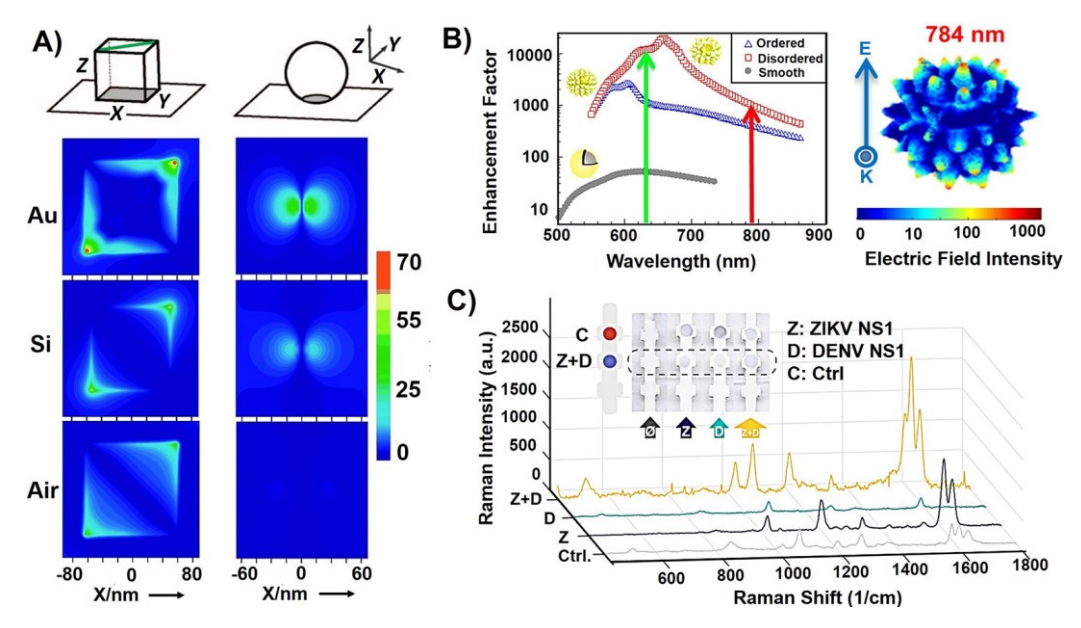


Figure 6. (A) Simulated E-field enhancements for a Ag nanocube and a nanosphere on Au, Si, and Air substrates using the discrete dipole approximation (DDA) method. For nanocube, the polarization direction of laser was along the green line. Reprinted with permission from ref 164. Copyright 2011 Wiley-VCH. (B) Calculated Raman enhancement factors for the ordered (blue), disordered (red), and smooth (gray) Au nanoshells based on the near-field intensities. The green and red arrows highlight laser excitation wavelengths. The 3D model on the right shows the E-field map (log scale) of an ordered nanoshell at 784 nm excitation wavelength. Reprinted with permission from ref 168. Copyright 2014 American Chemical Society. (C) Multiplexed detection of Zika virus (ZIKV) and Dengue virus (DENV) using SERS tags-based lateral flow assay. The SERS spectra were recorded from the test zones of four strips as shown in the inset. Adapted with permission from ref 169. Copyright 2017 American Chemical Society.

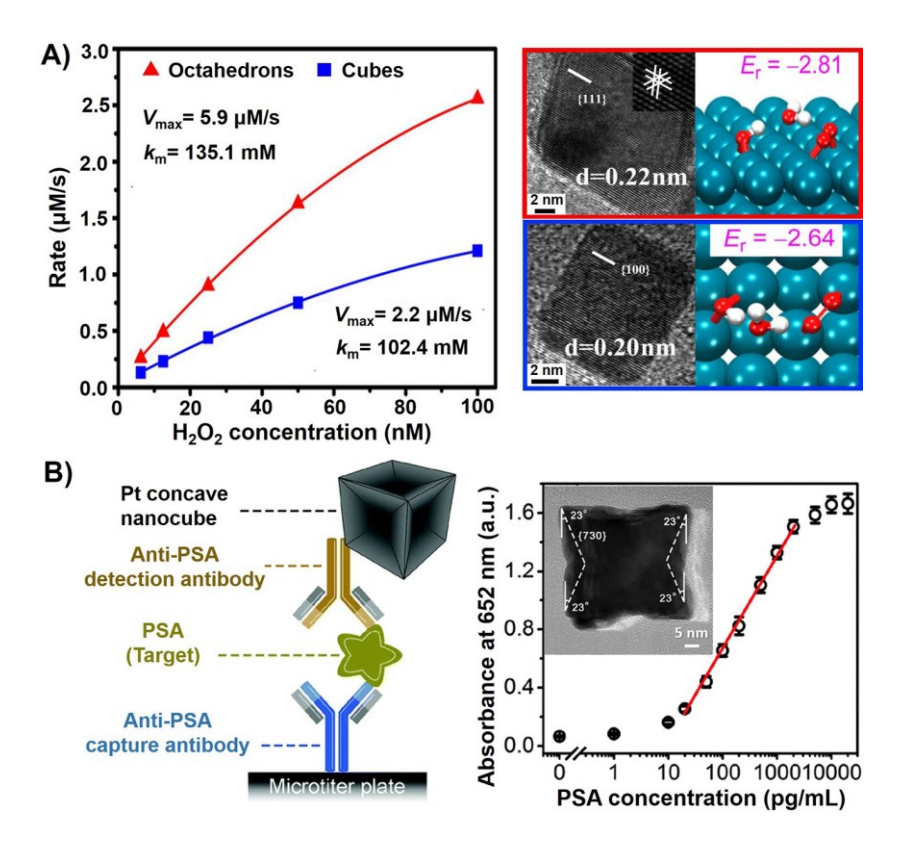


Figure 7. (A) Catalase-like activity of Pd octahedrons and nanocubes. The plots (left column) show the steady-state kinetic assay of Pd nanostructures with H_2O_2 . V_{max} and K_m in the inset indicate the maximal reaction velocity and the Michaelis-Menten constant, respectively. The right column shows high-resolution TEM (HRTEM) images of individual Pd octahedron (top) and nanocube (bottom). The models show simulated atomic structures on metal surfaces after the reaction of $H_2O_2 + HO_2 \rightarrow O_2 + OH + H_2O$. E_r is the reaction energy. Adapted with permission from ref 174. Copyright 2016 American Chemical Society. (B) ELISA of prostate specific antigen (PSA) using Pt concave nanocubes as the labels, which act as peroxidase mimics to generate color signal by catalyzing chromogenic substrates. Left column shows the schematic illustration of the assay. Right column shows the calibration curve of the assay for PSA standards. The inset shows TEM image of an individual Pt concave nanocube. Adapted with permission from ref 177. Copyright 2017 Royal Society of Chemistry.

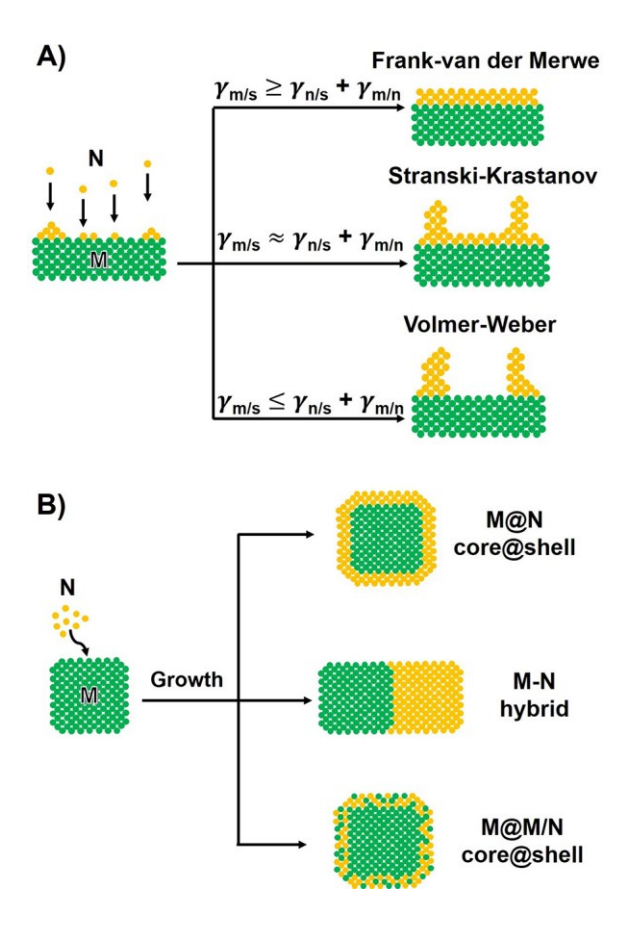


Figure 8. (A) Three possible growth modes for the deposition of metal N atoms on the surface of a seed made of metal M. (B) Three representative types of bimetallic nanostructures with different elemental distributions that are formed through the growth of a cubic seed under the layer-by-layer mode.

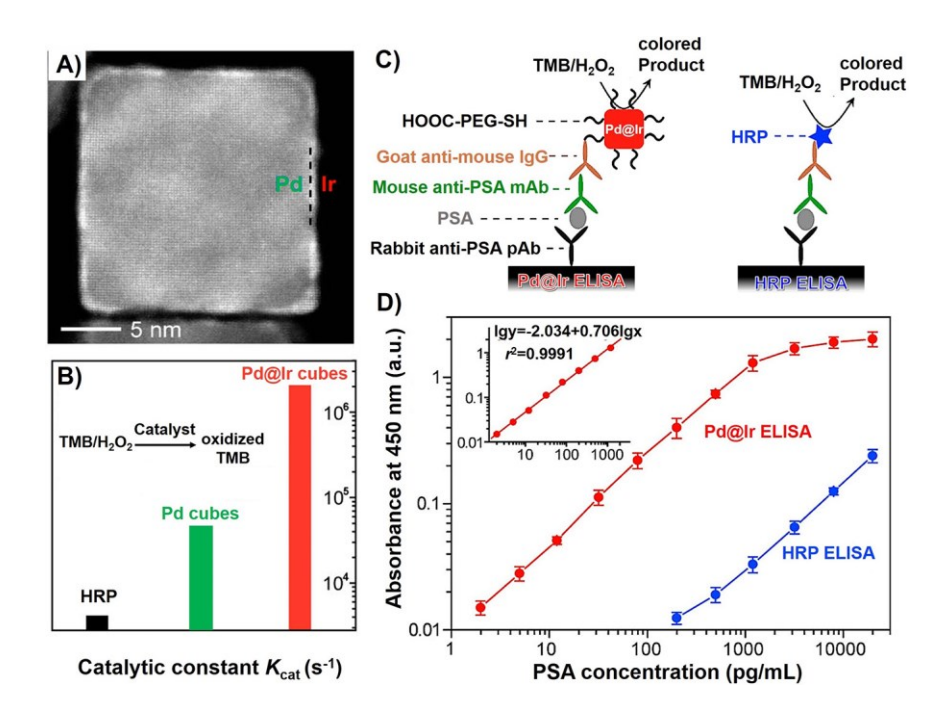


Figure 9. Pd@Ir_{1-2L} core@shell cubes and their use in ELISA. (A) High-angle annular dark-field scanning TEM (HAADF-STEM) image of an individual Pd@Ir_{1-2L} cube. (B) A chart comparing the peroxidase-like efficiencies (in terms of K_{cat}) of HRP, Pd cubes, and Pd@Ir_{1-2L} cubes. (C) Schematics showing the principles of Pd@Ir_{1-2L} cube- and HRP-based ELISAs. (D) Calibration curves of the two ELISAs for PSA standards. Inset shows the linear range region of the Pd@Ir_{1-2L} cube-based ELISA. Adapted with permission from ref 194. Copyright 2015 American Chemical Society.

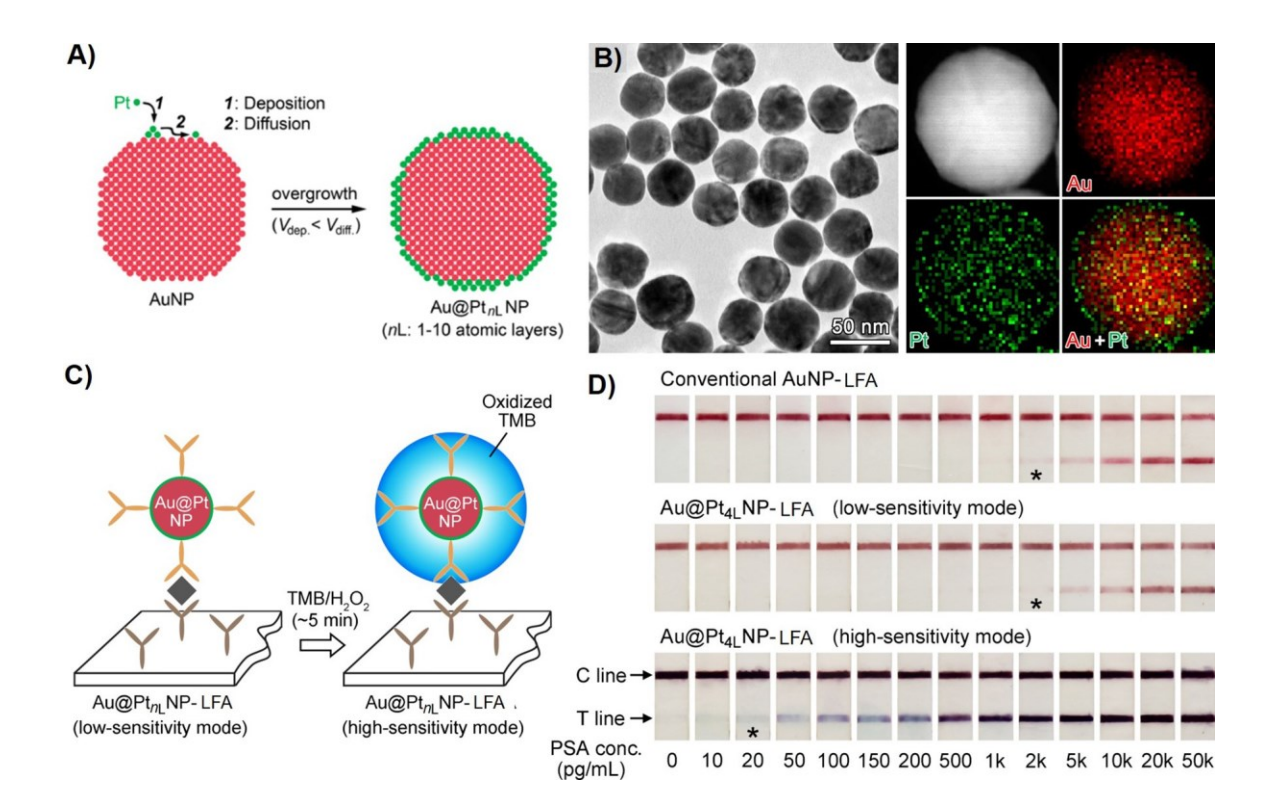


Figure 10. Au@Pt_{nL} NPs (*n*L: *n* atomic layers) and their use in LFA. (A) Schematics showing the preparation of Au@Pt_{nL} NPs, where Pt atoms are deposited on AuNP seeds to form conformal shells with smooth surfaces. (B) TEM (left) and energy-dispersive X-ray (EDX) mapping image (right) of Au@Pt_{4L} NPs as a representative sample. (C) Schematics showing the use of Au@Pt_{nL} NPs as labels for LFA. (D) Detection results of PSA standards by conventional AuNP-based LFA and Au@Pt_{4L} NP-based LFA under two different modes. The asterisks (*) indicate limits of detection by the naked eye. Adapted with permission from ref 197. Copyright 2017 American Chemical Society.

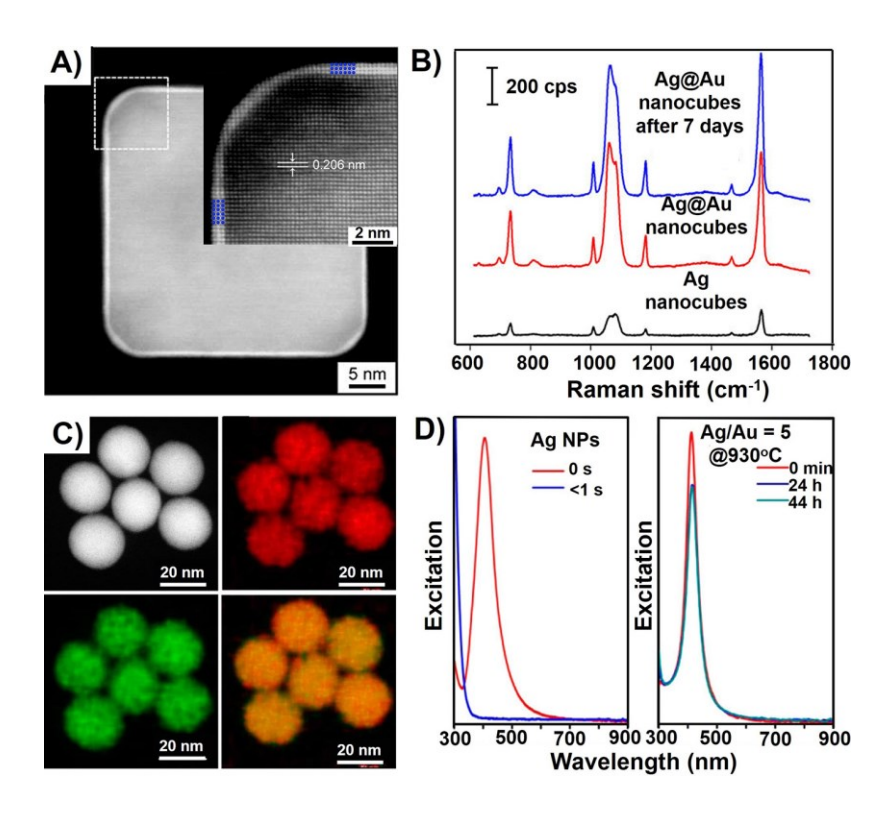


Figure 11. (A) HAADF-STEM image of an individual Ag@Au core@shell nanocube. Inset is a magnified image highlighting the three atomic layers of Au on the Ag core. (B) SERS spectra taken from aqueous suspensions of 1,4-benzenedithiol functionalized Ag@Au nanocubes (sample in (A)) and Ag nanocubes. Adapted with permission from ref 206. Copyright 2014 American Chemical Society. (C) STEM and EDX mapping images of Ag/Au alloyed NPs (Ag/Au = 5). (D) UV-vis spectra recorded from pure Ag NPs and Ag/Au alloyed NPs that were suspended in a mixed solvent of H₂O₂ and ammonia. Reprinted with permission from ref 207. Copyright 2014 American Chemical Society.

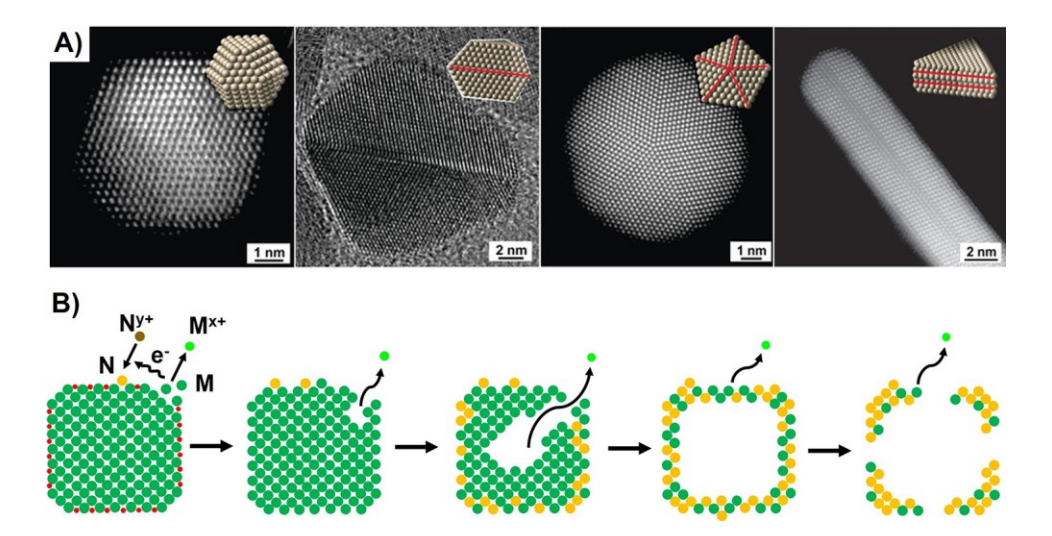


Figure 12. (A) Electron microscope images together with 3D models showing four representative types of *fcc* metal nanostructures with different crystallinities (from left to right): single-crystal cuboctahedron, singly twinned right bipyramid, multiply twinned decahedron, and stacking fault-contained triangular nanoplate. Red lines in the models denote twin boundaries or stacking faults. Adapted with permissions from refs 107, 148, 208 and 209. Copyright 2017 Wiley-VCH, 2013, 2012, and 2015 American Chemical Society, respectively. (B) Schematics illustrating the morphological and compositional changes during the galvanic replacement between a cubic template of metal M and ions of metal N. The red dots on template denote capping agents.

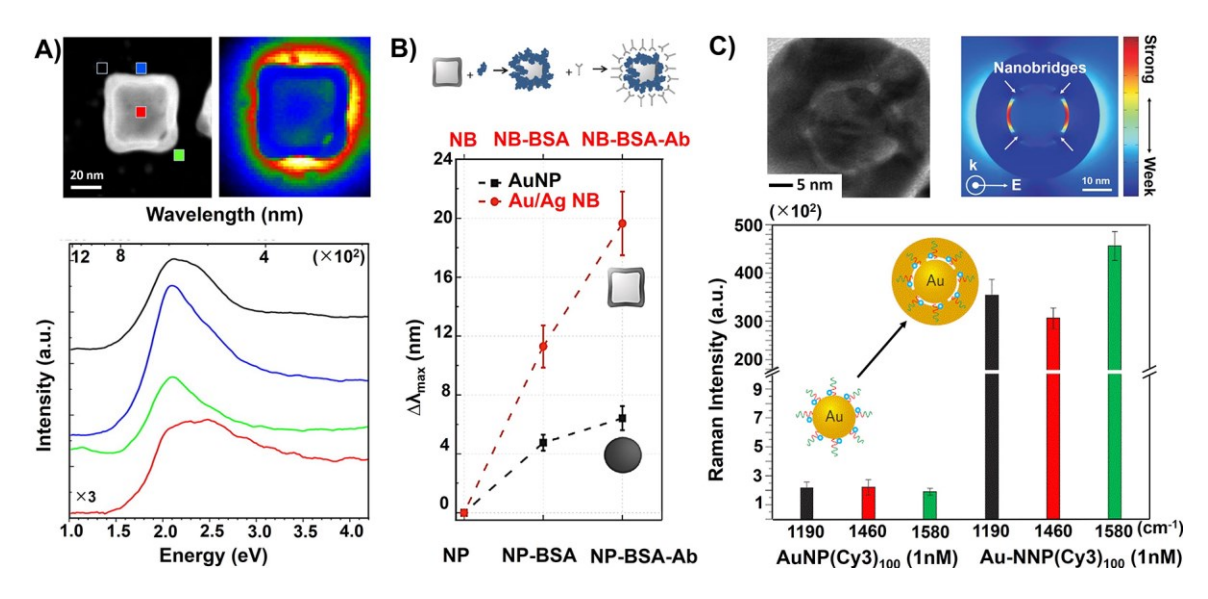


Figure 13. (A) Plasmonic properties of Au/Ag nanoboxes (NBs). HAADF-STEM image of a single Au/Ag NB (top left), selected area EEL spectra of the areas marked in the HAADF-STEM image (bottom), and abundance map obtained by vertex component analysis (VCA) processing (top right). (B) The shifts of major LSPR peaks (Δλ_{max}) for Au/Ag NB and AuNP suspensions after they had been conjugated with BSA and then anti-BSA antibody (BSA-Ab). (C) Au nanobridged nanogap particles (Au-NNPs) that were prepared using dye-DNA modified AuNPs as the seeds. TEM image of a single Au-NNP (top left), calculated near-field electromagnetic field distribution of a Au-NNP (top right), and a chart comparing the Raman intensities of Cy3 dyes modified AuNPs and AuNNPs in solution. (A) and (B) were adapted with permission from ref 240. Copyright 2016 American Chemical Society. (C) was adapted with permission from ref 242. Copyright 2011 Nature Publishing Group.

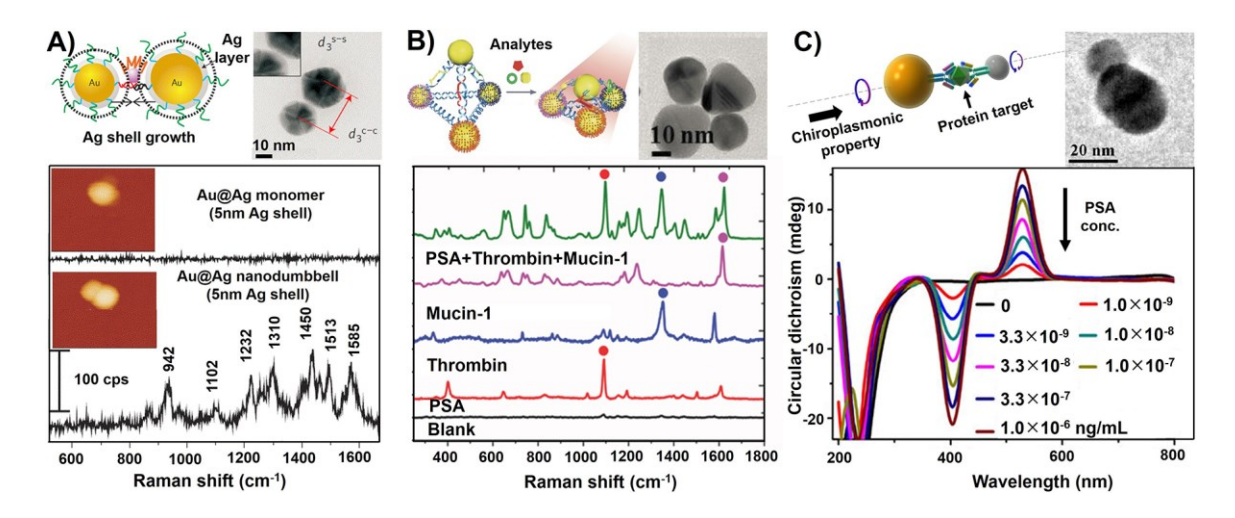


Figure 14. (A) Au@Ag nanodumbbells. Schematics (top left), TEM image (top right), and SERS spectra recorded from Cy3 dyes modified individual Au@Ag monomer and Au@Ag nanodumbbell (bottom). Adapted with permission from ref 247. Copyright 2010 Nature Publishing Group. (B) SERS encoded AgNP pyramids for multiplexed detection. Schematics showing the principle of detection (top right), TEM image of a single AgNP pyramid (top right), and results for multiplexed detection of PSA, mucin-1, and thrombin. Reprinted with permission from ref 248. Copyright 2015 Wiley-VCH. (C) Dimer of AuNP and AgNP for chiroplasmonic detection. Schematics showing the assembly of dimer and the detection principle (top left), TEM image of a dimer (top right), and detection results for PSA at different concentrations (bottom). Adapted with permission from ref 249. Copyright 2013 American Chemical Society.



Figure 15. (A) Controlled growth of AuNPs for bioanalysis. The enzyme linked with analytes governs the growth pathway of AuNPs by controlling the concentration of H₂O₂ as reductant for Au³⁺. AuNPs with different morphologies display diverse colors as detection signal for bioanalysis. Adapted with permission from ref 251. Copyright 2012 Nature Publishing Group. (B) Controlled growth of Ag on Au nanobipyramids as seeds for bioanalysis. The enzyme linked with analytes generates 4-aminophenol as reductant for Ag⁺ ions. Au nanobipyramids coated with various amount of Ag show different colors. Adapted with permission from ref 252. Copyright 2016 American Chemical Society. (C) Controlled etching of Ag nanoplates for bioanalysis. The enzyme linked with analytes produces H₂O₂ that can etch Ag nanoplates. The size reduction and shape change of Ag nanoplates during etching result in sensitive SPR shift. Adapted with permission from ref 254. Copyright 2014 American Chemical Society.